

Research article

Multi-stage crustal melting from Late Permian back-arc extension through Middle Triassic continental collision to Late Triassic post-collisional extension in the East Kunlun Orogen



Xu Zhao ^{a,b}, Junhao Wei ^{a,*}, Lebing Fu ^{a,*}, Jan Marten Huizenga ^{b,c}, M. Santosh ^{d,e,f}, Jiajie Chen ^g, Dianzhong Wang ^h, Aobing Li ^a

^a School of Earth Resources, China University of Geosciences, Wuhan 430074, China

^b Economic Geology Research Institute (EGRU), College of Science and Engineering, James Cook University, Townsville, Queensland 4811, Australia

^c Department of Geology, University of Johannesburg, PO Box 524, Auckland Park 2006, South Africa

^d School of Earth Science and Resources, China University of Geosciences, Beijing 100083, China

^e Department of Earth Sciences, University of Adelaide, Adelaide, SA 5005, Australia

^f Yonsei Frontier Lab, Yonsei University, Seoul, Republic of Korea

^g School of Earth Science, East China University of Technology, Nanchang 330013, China

^h State Key Laboratory of Ore Deposit Geochemistry, Institute of Geochemistry, Chinese Academy of Sciences, Guiyang 550081, China

ARTICLE INFO

Article history:

Received 29 November 2019

Received in revised form 22 February 2020

Accepted 22 February 2020

Available online 26 February 2020

Keywords:

East Kunlun Orogen

S-type granite

Paleo-Tethys Ocean

Back-arc basin

Continental collision

Post-collisional extension

ABSTRACT

The East Kunlun Orogen is an important part of the East Tethys region and has received significant attention with regards to the evolution of the Tethys Ocean. This contribution presents geochronological, whole-rock major and trace element geochemical, and Sr-Nd-Hf isotopic data of magmatic rocks within the Kengdenongshe polymetallic deposit in the eastern part of the East Kunlun Orogen. Here, we report zircon U-Pb ages of ca. 257 Ma and ca. 211 Ma for granite porphyry intrusions, and ca. 240 Ma for the rhyolitic tuff. These rocks are characterized by high SiO₂, variable Al₂O₃ and K₂O, low Na₂O, MgO and CaO contents, and high A/CNK ratios, which is typical of S-type granitic rocks. They exhibit large-ion lithophile element enrichment, depletion of high field strength elements, have low (La/Yb)_N ratios, and negative Eu anomalies. They also display variable (⁸⁷Sr/⁸⁶Sr)_i ratios (0.709981 to 0.720907), negative ε_{Nd} (t) values (-8.7 to -5.5), and a wide (enriched) zircon ε_{Hf} (t) range (-10.1 to -0.8). The geochemical and isotope data indicate magma derivation through dehydration melting of heterogeneous crustal sources including clay-poor meta-sedimentary rocks and amphibolite, which are both parts of the East Kunlun Orogen basement. These results provide evidence for the evolution of the Paleo-Tethys Ocean in the East Kunlun Orogen including Late Permian (266–255 Ma) back-arc extension, Late Permian to Middle Triassic (255–240 Ma) subduction, Middle Triassic (240–225 Ma) continental collision, and Late Triassic (<225 Ma) post-collisional extension. This study further suggests that the 257 Ma and 211 Ma granite porphyries are related to the asthenosphere upwelling in a back-arc basin and post-collision extensional setting, respectively. The 240 Ma rhyolitic tuff is linked to anatexis associated with crustal thickening during continental collision.

© 2020 Elsevier B.V. All rights reserved.

1. Introduction

S-type granites are common constituents of collisional orogens and are considered to be the markers of continental collision or post-collisional events, as crustal thickening during continental collision and post-collisional asthenospheric upwelling can induce crustal melting that is a key factor for generating S-type granitic rocks (e.g. Barbarin, 1999; Liu and Zhao, 2018; Sylvester, 1998; Vernon, 1984). It

has also been suggested that S-type granites could form in a back-arc basin setting, explaining the generation of S-type granites in Circum-Pacific orogens (Collins and Richards, 2008). S-type granites can provide insights into the mechanism of crustal melting and help to further constrain the geodynamic processes of back-arc extension, continental collision, and post-orogenic extension (Collins and Richards, 2008; Sylvester, 1998).

The East Kunlun Orogen (EKO) is one of the major tectonic-magmatic belts in the East Tethys domain. It records the history of terrane accretion between Gondwana and Laurasia (Harris et al., 1988) and the evolution of the Proto-Tethys Ocean in the Early Paleozoic and the Paleo-Tethys Ocean during the Late Paleozoic to Mesozoic (Sengör,

* Corresponding authors at: School of Earth Resources, China University of Geosciences, Lumo Road No. 388, Hongshan District, Wuhan 430074, Hubei Province, China.

E-mail addresses: junhao@163.com (J. Wei), fub@cug.edu.cn (L. Fu).

1979; Suess, 1981; Yin and Harrison, 2000; Mo et al., 2007; Liu et al., 2017; Wu et al., 2019). The opening of the Paleo-Tethys Ocean at 345–333 Ma in the EKO is indicated by the presence of Carboniferous ophiolites in the South Eastern Kunlun Suture (SEKS). Initial subduction of the Paleo-Tethys Ocean before 278 Ma is evidenced by Early Permian arc magmatism (Chen et al., 2001; Xiong, 2014). Numerous Late Permian to Triassic granitic rocks that were generated during the tectonic-magmatic events associated with the Paleo-Tethys Ocean subduction and subsequent continental collision are widely distributed in this region (Fig. 1; Ma et al., 2015; Chen et al., 2016; Dong et al., 2018; Xiong et al., 2019). Late Permian to Early Triassic calc-alkaline granite and granodiorite with mafic magmatic enclaves are interpreted to have a mixed source of oceanic slab and subcontinental mantle (Mo et al., 2007; Xiong, 2014; Xiong et al., 2014). The Middle to Late Triassic medium to high-K granitic rocks were mainly sourced from melting of oceanic slab or the lower continental crust during continental collision (Huang et al., 2014; Wang et al., 2009). The evolutionary model of single subduction in the Late Permian to Middle Triassic followed by Middle Triassic continental collision has been established by studies on regional magmatism (Chen et al., 2017; Xiong, 2014). However, the occurrence

of regional mafic rocks and sedimentary units indicates that Late Permian back-arc extension was followed by continuous Late Permian to Triassic subduction (Xiong et al., 2011; Zhao et al., 2019). A detailed study of Late Permian to Triassic S-type granites in the EKO will provide a better understanding of (1) the tectonic evolution of the Paleo-Tethys Ocean, and (2) crustal melting processes in different tectonic settings including back-arc extension and continental collision.

Late Permian to Triassic S-type granitic rocks were recently identified in the Kengdenongshe polymetallic deposit within the Gouli field in eastern EKO (Fig. 2), which is the only known giant Au-Ag-Pb-Zn polymetallic ore in the EKO. These S-type granitic rocks include the Late Permian granite porphyry (Fig. 3, in drill core), Middle Triassic rhyolitic tuff, and Late Triassic granite porphyry (Fig. 3). Previous studies showed that the mineralization is spatially and genetically associated with Late Permian granite porphyry and Middle Triassic rhyolitic tuff (Xia, 2017). Therefore, these magmatic rocks can provide information on the tectonic setting and the genesis of the polymetallic deposit.

In this contribution, we present zircon U–Pb age, major and trace element geochemical, and Sr-Nd-Hf isotopic data of the Late Permian granite porphyry, ore-hosting Middle Triassic rhyolitic tuff, and Late

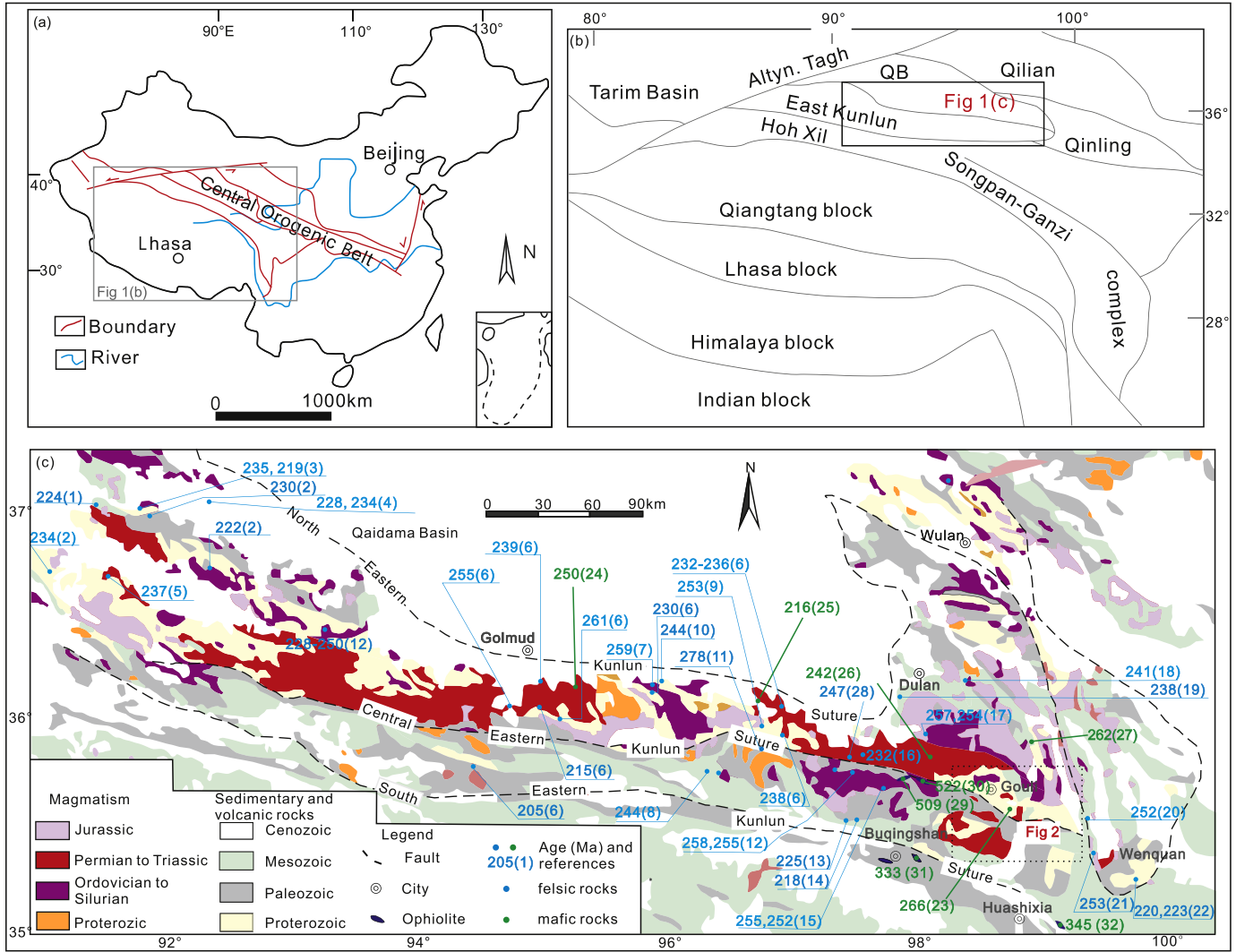


Fig. 1. Geological map showing tectonic location (a,b) and framework of the EKO (c). QB: Qaidama Basin. The data sources are as follows: 1: Xiao et al. (2013); 2–3: Feng et al. (2010); 4: Gao et al. (2012); 5: (16) Wang et al. (2009); 6: Xiong et al. (2014); 7: Xiong et al. (2014); 8: Liu et al. (2012); 9: Xiong et al. (2013); 10: Ding et al. (2011); 11: Ma et al. (2015); 12: Zhang (2012) 13, 16: Xia et al. (2014); 14: Chen et al. (2013); 15: Sun (2010); 17: He et al. (2016); 18: Chen et al. (2012); 19: Yin et al. (2013); 20: Xiong et al. (2014); 21: Dai et al. (2013); 22: Liu et al. (2012); 23: Zhao et al. (2019); 24: Xiong et al. (2011); 25: Liu et al. (2017); 26: Zhao et al. (2018); 27: Kong et al. (2017); 28: Li et al. (2018); 29: Lu et al. (2002); 30: Yang et al. (1996); 31: Chen et al. (2004); 32: Liu et al. (2011).

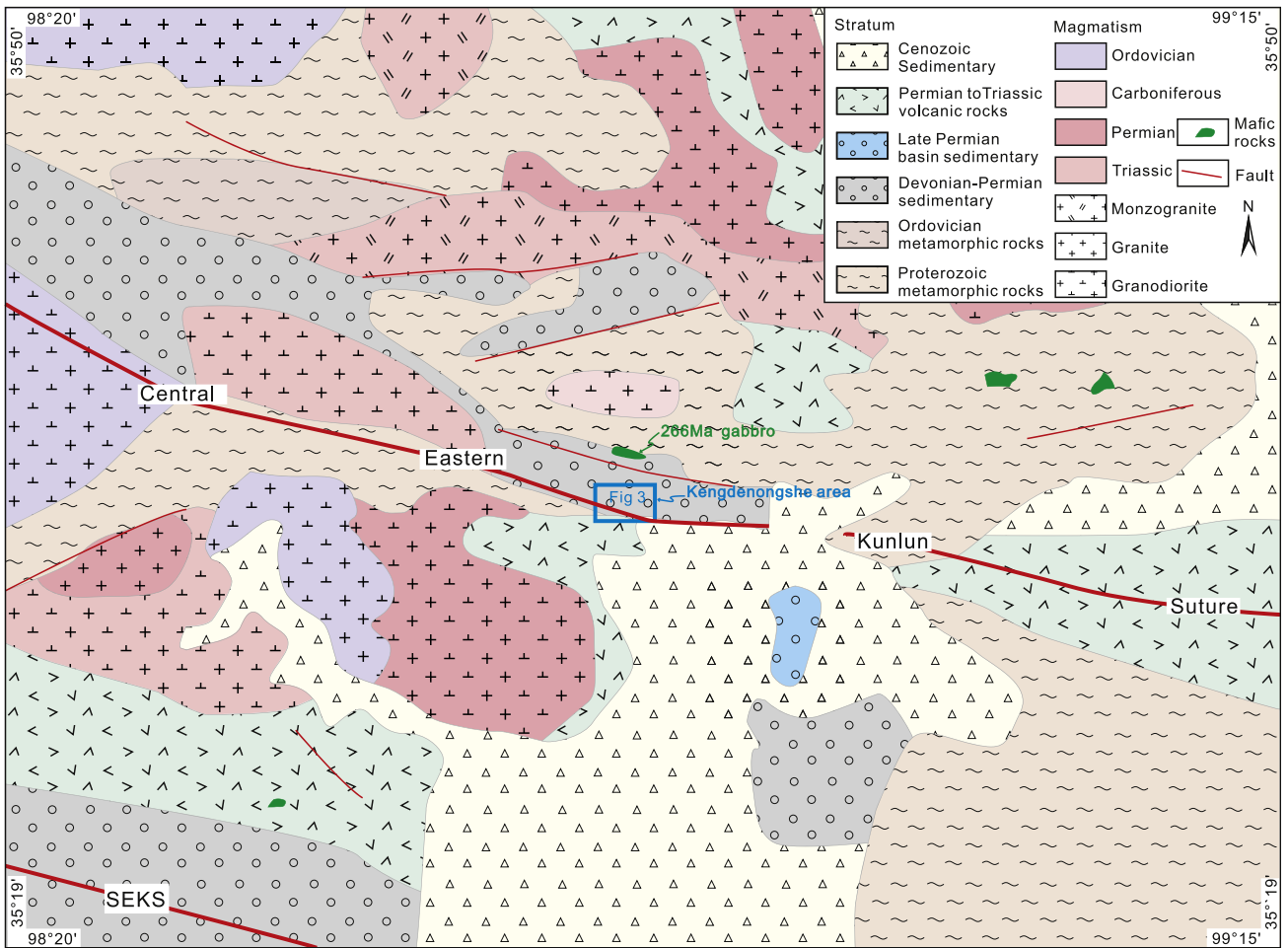


Fig. 2. Geological map of the Gouli field showing the location of the Kengdenongshe polymetallic deposit. The age of the gabbro in the northern part of the Kengdenongshe is from Zhao et al., 2019. SEKS: South Eastern Kunlun Orogen.

Triassic granite porphyry. The main objectives are to (1) obtain a better understanding of the petrogenesis and tectonic setting of these Late Permian to Triassic magmatic rocks, and (2) establish the evolution of the Paleo-Tethys Ocean in the EKO.

2. Geological background

2.1. Geology of the EKO and Gouli area

The EKO, which is an important part of the Tibetan plateau, is separated by the North Eastern Kunlun Suture Zone from the northern Qaidam Basin and by the Altyn fault belt from the western Tarim Basin. It borders the southern Hoh Xil–Songpan–Ganze complex and the eastern Qinling orogenic belt (Fig. 1a,b, Yang et al., 1996; Xu et al., 2015). Two regional faults run through the EKO, including the Central Eastern Kunlun Suture (CEKS) and the SEKS (Fig. 1c). These two suture belts are related to the closure of the Proto-Tethys Ocean in the Early Paleozoic and the Paleo-Tethys Ocean in Mesozoic, respectively (Dong et al., 2018). Early Cambrian (522–509 Ma) ophiolites in the CEKS record the opening of the Proto-Tethys whereas Early Carboniferous ophiolites (345–333 Ma) in the SEKS record the opening of the Paleo-Tethys Ocean (Fig. 1c, Yang et al., 1996; Chen et al., 2001).

The EKO basement comprises middle to high grade metamorphic rocks of the Paleoproterozoic Jinshikou Group (2366–1600 Ma, Wang et al., 2007; Chen et al., 2006; Zhang et al., 2003) and the Xiaomiao Formation (1600–1035 Ma, Chen et al., 2006; Jin et al., 2015; Wang et al., 2004). The major rocks types are paragneiss, amphibolite, marble,

orthogneiss, and migmatite (He et al., 2016), and are unconformably overlain by the weakly metamorphosed volcanic rocks of the Ordovician Naij-Tai Group and discontinuous Carboniferous to Jurassic sediments and volcanic rocks (Chen et al., 2017, Fig. 2).

Previous studies mainly focused on the regional Late Permian to Triassic magmatic rocks and include the following: (1) Late Permian gabbro derived from melting of upwelling asthenosphere in a back-arc basin (Zhao et al., 2019); (2) Late Permian to Early Triassic calc-alkaline granite and granodiorite with mixed source of slab and subcontinental mantle (Xiong, 2014; Cheng et al., 2017), and calc-alkaline mafic rocks derived from enriched mantle wedge in a subduction zone (Xiong et al., 2011; Zhao et al., 2018); (3) Middle to Late Triassic medium to high-K granitic rocks sourced from melting of oceanic slab or lower continental crust in a continental collision zone (Huang et al., 2014; Wang et al., 2009). (4) Late Triassic mafic dykes derived from partial melting of the asthenosphere (Liu et al., 2017), felsic rocks derived from the partial melting of the thickened lower continental crust (Ding et al., 2011; Luo et al., 2014; Yu et al., 2015) in a post-collision setting.

The Gouli area is located in the eastern margin of the EKO (Fig. 1c). NWW-trending structures, including the CEKS and SEKS, control the distribution of regional strata and magmatism in the Gouli district (Fig. 2). The basement rocks are comprised of Proterozoic mid- to high-grade metamorphic rocks and exposed throughout the region. The main geological units in the Gouli area from south to north are the SEKS, Late Permian to Triassic volcanic rocks and granitic intrusions, the CEKS, Kengdenongshe back-arc basin gabbro and the S-type

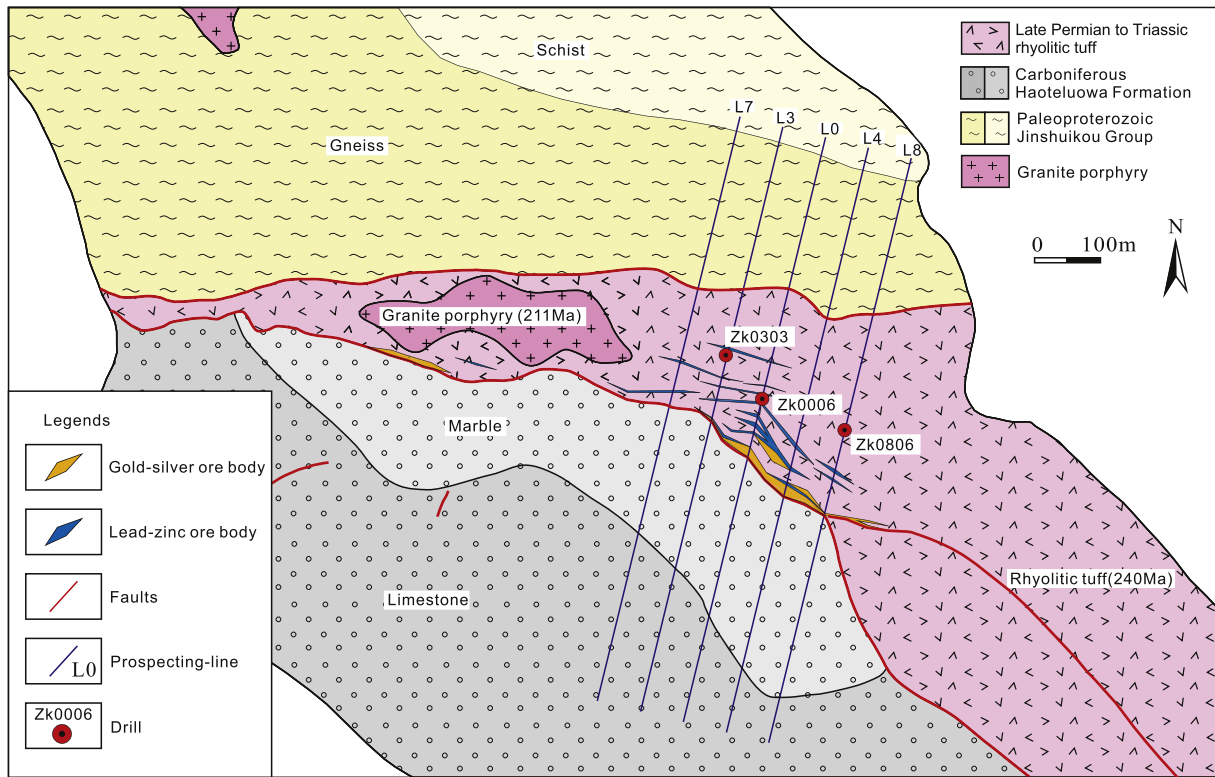


Fig. 3. Simplified geological map of the Kengdenongshe area.

granites, and extensive Triassic intrusions. The SEKS in the most southern area (Fig. 2) represents the suture belt. The Late Permian to Triassic volcanic rocks and granitic intrusions in north of the SEKS comprise the magmatic assemblage. The Kengdenongshe back-arc basin gabbro near the CEKS suggests the back-arc basin. The extensive Triassic intrusions in the north of the CEKS compose the continental arc crust (Chen et al., 2017; Ma et al., 2015; Xiong, 2014; Zhao et al., 2019).

2.2. Geology of the Kengdenongshe area

The Kengdenongshe area is characterized by WNW-trending faults, which control the distribution of the strata and ore bodies (Fig. 3). The ore bodies are hosted within the Late Permian to Triassic rhyolitic tuff. The tuff is bordered to the south by limestone and marble of the Carboniferous Haoteluowa Formation, and to the north by schist and gneiss of the Paleoproterozoic Jinshukou Group (Fig. 3). Both the Haoteluowa Formation and Jinshukou Group are separated from the tuff by northeast dipping thrust faults, which are several kilometers long and ca. 20 m wide. Late Permian granite porphyries intruded into the Jinshukou Group gneiss and exposed in the northern part of the Kengdenongshe area, but they were mainly found in drill core (Fig. 3). The tuff layer trends E-W for more than 8 km, with a width of more than 1 km. Late Triassic granite porphyry intruded the tuff and is exposed in the Kengdenongshe area for about 400m².

3. Petrography and analytical methods

Late Permian granite porphyry found in the drill core (ZK305, Fig. 3) is purple to red in hand specimen and exhibits porphyritic texture (Fig. 4a), with quartz (30 vol%), plagioclase (15 vol%), and K-feldspar (5 vol%) phenocrysts embedded in a fine-grained quartz and plagioclase groundmass (50 vol%) (Fig. 4d–g). The plagioclase phenocrysts (3–4 mm) form subhedral laths with occasional twinning. The K-

feldspar phenocrysts (up to 6 mm) are usually subhedral to euhedral. Accessory minerals include zircon, titanite, biotite, and sericite (less than 5 vol%), and sericite occurs as an alteration product near the orebodies.

The tuff is grey to green in hand specimen (Fig. 4b) and comprises less than 2 mm sized subhedral to euhedral quartz (25–30 vol%), plagioclase (10–15 vol%), and K-feldspar (5–10 vol%) phenocrysts in a felsic groundmass (40–45%) with accessory zircon, titanite and Fe–Ti oxides and slight alteration mineral of barite (Fig. 4h–k).

The Late Triassic granite porphyry is pale red to green in hand specimen and exhibits porphyritic texture (Fig. 4c). The samples contain subhedral to euhedral quartz (30 vol%), plagioclase (5 vol%) and K-feldspar (5 vol%) phenocrysts (1–3 mm) (Fig. 4l–o). The phenocrysts are hosted in a groundmass of quartz (40%) and plagioclase (20%) with accessory magnetite, apatite, zircon, and biotite (less than 5 vol%).

After the petrographic examination, zircons were picked for zircon U–Pb dating and in-situ Lu–Hf isotopic analysis. Fresh whole-rock samples were powdered to less than a 200-mesh size for whole-rock major and trace element geochemistry and Sr–Nd isotopic analyses. Detailed analytical procedures and methods are presented in Appendix A.

4. Results

4.1. Zircon U–Pb geochronology

Cathodoluminescence images and U–Pb isotopic data for the zircon grains from granite porphyries and rhyolitic tuff are shown in Table 1 and Figs. 5 and 6. The samples of Late Permian granite porphyry come from drill core ZK305 (Fig. 3). The zircon grains are colorless, mostly ellipsoidal shaped with lengths between 50 and 150 µm (length-width ratios between 1 and 3) (Fig. 5a). The grains exhibit clear oscillatory zoning and Th/U ratios of 0.54–1.41, compared with typical features of magmatic zircons (Hoskin and Schaltegger, 2003). All data plots close

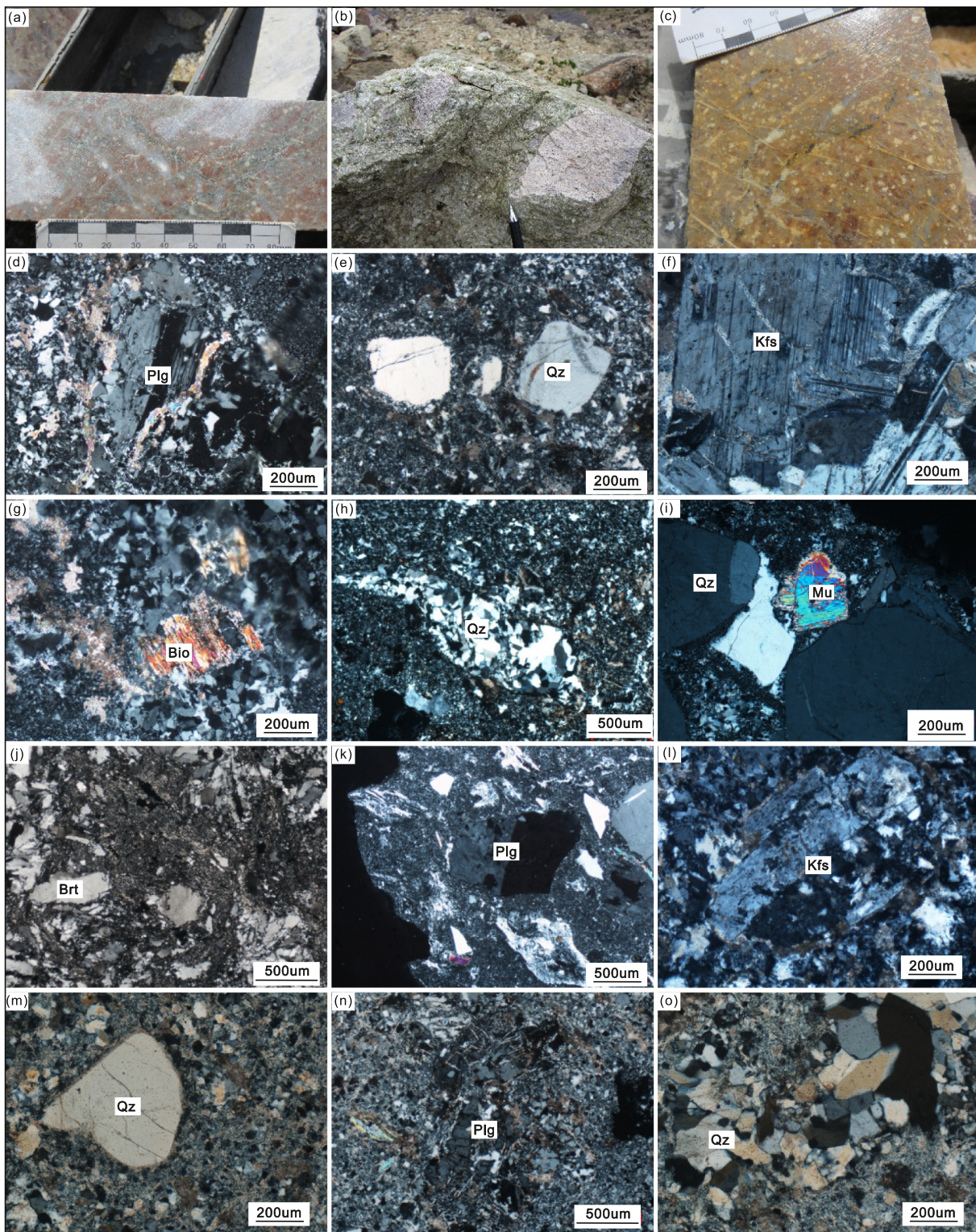


Fig. 4. Representative photos and photomicrographs of the Late Permian granite porphyry (a, d–g), Middle Triassic rhyolitic tuff (b, h–k) and Late Triassic granite porphyry (c, l–o). Plg = plagioclase; Qz = quartz; Kfs = K-feldspar; Bio = biotite; Mu = muscovite; Brt = barite.

to the U–Pb Concordia line (Fig. 6a,b), yielding a weighted average mean age of 257 ± 2 Ma (MSWD = 0.48).

Zircon grains from rhyolitic tuff are light yellow, euhedral columnar shaped crystals with lengths between 70 and 200 μm and length-width ratios between 1 and 3 (Fig. 5b). They display clear oscillatory zoning and varying Th/U ratios of 0.49–1.58, indicative of a magmatic origin (Hoskin and Schaltegger, 2003). Sixteen data points yield a concordant

age of 240 ± 2 Ma (MSWD = 0.74, Fig. 6c,d), which is the same as the weighted mean $^{206}\text{Pb}/^{238}\text{U}$ age.

Zircon grains in Late Triassic granite porphyry are similar to those in Late Permian granite porphyry with regards to shape, size, and length-to-width ratio. However, they appear darker in the cathodoluminescence images (Fig. 5c). They exhibit clear oscillatory zoning and have Th/U ratios of 0.48–1.43, indicating their magmatic origin

Table 1

LA-ICP-MS zircon U-Pb dating data of the Kengdenongshe granite porphyries and rhyolitic tuff.

Sample No	Th ppm	U ppm	Th/U	U-Th-Pb isotopic ratio								Age (Ma)							
				$^{207}\text{Pb}/^{206}\text{Pb}$	1 σ	$^{207}\text{Pb}/^{235}\text{U}$	1 σ	$^{206}\text{Pb}/^{238}\text{U}$	1 σ	$^{208}\text{Pb}/^{232}\text{Th}$	1 σ	$^{207}\text{Pb}/^{206}\text{Pb}$	1 σ	$^{207}\text{Pb}/^{235}\text{U}$	1 σ	$^{206}\text{Pb}/^{238}\text{U}$	1 σ	$^{208}\text{Pb}/^{232}\text{Th}$	1 σ
B0305-1 (Late Permian granite porphyry)																			
1	513	929	0.55	0.0720	0.0019	0.4008	0.0120	0.0404	0.0005	0.0179	0.0005	985	52	342	9	255	3	358	9
2	328	520	0.63	0.0610	0.0014	0.3447	0.0098	0.0410	0.0005	0.0152	0.0004	640	50	301	7	259	3	305	8
3	305	566	0.54	0.0609	0.0014	0.3426	0.0096	0.0408	0.0005	0.0156	0.0004	634	49	299	7	258	3	312	8
4	284	390	0.73	0.0676	0.0018	0.3792	0.0119	0.0407	0.0006	0.0168	0.0006	856	55	327	9	257	3	336	12
5	766	543	1.41	0.0625	0.0019	0.3534	0.0122	0.0410	0.0006	0.0135	0.0004	692	65	307	9	259	4	271	7
6	440	815	0.54	0.0682	0.0017	0.3809	0.0111	0.0405	0.0005	0.0173	0.0005	875	49	328	8	256	3	347	10
7	712	1172	0.61	0.0915	0.0021	0.5149	0.0146	0.0408	0.0005	0.0227	0.0007	1456	44	422	10	258	3	453	13
8	781	1294	0.60	0.0928	0.0024	0.5190	0.0158	0.0406	0.0006	0.0227	0.0007	1483	49	425	11	257	3	453	14
9	630	1155	0.55	0.0636	0.0017	0.3512	0.0110	0.0401	0.0006	0.0167	0.0004	728	55	306	8	253	3	335	8
10	423	481	0.88	0.0539	0.0014	0.3053	0.0094	0.0411	0.0006	0.0129	0.0003	367	58	271	7	260	3	260	6
11	689	713	0.97	0.0692	0.0017	0.3877	0.0114	0.0406	0.0006	0.0150	0.0004	905	50	333	8	257	3	300	8
12	297	459	0.65	0.0625	0.0017	0.3520	0.0109	0.0409	0.0006	0.0156	0.0004	690	55	306	8	258	3	312	9
13	679	1024	0.66	0.0566	0.0014	0.3145	0.0095	0.0403	0.0006	0.0141	0.0004	476	55	278	7	255	3	282	8
14	702	1239	0.57	0.0585	0.0016	0.3257	0.0102	0.0404	0.0006	0.0159	0.0005	547	57	286	8	256	3	318	10
B0808-5-6 (Rhyolitic tuff)																			
1	314	343	0.92	0.0546	0.0016	0.2889	0.0097	0.0384	0.0005	0.0128	0.0005	396	63	258	8	243	3	258	10
2	794	1069	0.74	0.0778	0.0019	0.4036	0.0121	0.0376	0.0005	0.0180	0.0007	1142	48	344	9	238	3	361	14
3	726	1042	0.70	0.1057	0.0036	0.5636	0.0208	0.0387	0.0006	0.0231	0.0010	1727	60	454	14	245	4	461	19
4	764	1295	0.59	0.0565	0.0015	0.2960	0.0092	0.0380	0.0005	0.0148	0.0006	470	57	263	7	241	3	298	12
5	782	1148	0.68	0.0869	0.0025	0.4421	0.0146	0.0369	0.0005	0.0189	0.0008	1358	54	372	10	234	3	378	16
6	1371	1869	0.73	0.1241	0.0030	0.6457	0.0190	0.0378	0.0005	0.0255	0.0011	2016	42	506	12	239	3	508	22
7	499	1019	0.49	0.0623	0.0017	0.3253	0.0105	0.0379	0.0005	0.0151	0.0007	686	57	286	8	240	3	304	14
8	252	456	0.55	0.0678	0.0025	0.3524	0.0142	0.0377	0.0006	0.0151	0.0008	862	75	307	11	239	4	304	15
9	426	574	0.74	0.1145	0.0038	0.5955	0.0220	0.0377	0.0006	0.0204	0.0011	1872	59	474	14	239	4	408	21
10	548	970	0.56	0.0786	0.0021	0.4137	0.0133	0.0382	0.0005	0.0200	0.0011	1163	53	352	10	242	3	401	21
11	768	1320	0.58	0.1098	0.0026	0.5721	0.0163	0.0378	0.0005	0.0278	0.0008	1796	43	459	11	239	3	554	15
12	2090	1324	1.58	0.1355	0.0031	0.7111	0.0198	0.0381	0.0005	0.0177	0.0005	2171	39	545	12	241	3	354	10
13	1115	1526	0.73	0.1489	0.0033	0.7925	0.0217	0.0386	0.0005	0.0302	0.0009	2334	38	593	12	244	3	602	18
14	942	1531	0.61	0.0717	0.0016	0.3694	0.0103	0.0374	0.0005	0.0184	0.0006	977	46	319	8	237	3	369	11
15	776	1261	0.62	0.0724	0.0020	0.3732	0.0117	0.0374	0.0005	0.0157	0.0005	998	54	322	9	237	3	314	11
16	585	1013	0.58	0.1315	0.0031	0.6921	0.0200	0.0382	0.0005	0.0390	0.0015	2118	41	534	12	242	3	774	29
B0008-1-4 (Late Triassic granite porphyry)																			
1	500	798	0.63	0.0578	0.0018	0.2639	0.0094	0.0331	0.0005	0.0229	0.0006	523	69	238	8	210	3	458	12
2	756	1293	0.58	0.0596	0.0014	0.2749	0.0080	0.0335	0.0005	0.0140	0.0004	588	50	247	6	212	3	282	7
3	520	1080	0.48	0.0573	0.0014	0.2652	0.0079	0.0336	0.0005	0.0136	0.0004	501	53	239	6	213	3	272	7
4	872	1376	0.63	0.0556	0.0012	0.2529	0.0071	0.0330	0.0005	0.0132	0.0004	435	49	229	6	209	3	264	7
5	430	719	0.60	0.0771	0.0018	0.3521	0.0102	0.0331	0.0005	0.0146	0.0004	1124	46	306	8	210	3	293	8
6	616	764	0.81	0.0780	0.0025	0.3649	0.0129	0.0339	0.0005	0.0169	0.0005	1148	62	316	10	215	3	339	11
7	1149	1437	0.80	0.0570	0.0013	0.2617	0.0073	0.0333	0.0005	0.0120	0.0004	490	48	236	6	211	3	242	7
8	656	1161	0.57	0.0571	0.0018	0.2624	0.0092	0.0333	0.0005	0.0104	0.0004	496	68	237	7	211	3	209	7
9	1256	1310	0.96	0.0666	0.0015	0.3059	0.0085	0.0333	0.0005	0.0119	0.0003	826	45	271	7	211	3	238	5
10	853	932	0.92	0.0525	0.0016	0.2425	0.0084	0.0335	0.0005	0.0114	0.0003	307	68	220	7	212	3	230	6
11	330	687	0.48	0.0537	0.0017	0.2508	0.0089	0.0339	0.0005	0.0105	0.0003	360	70	227	7	215	3	212	6
12	1228	861	1.43	0.0662	0.0017	0.3044	0.0094	0.0334	0.0005	0.0111	0.0003	811	53	270	7	212	3	223	6
13	578	900	0.64	0.0543	0.0022	0.2568	0.0109	0.0343	0.0005	0.0125	0.0004	381	86	232	9	218	3	251	8

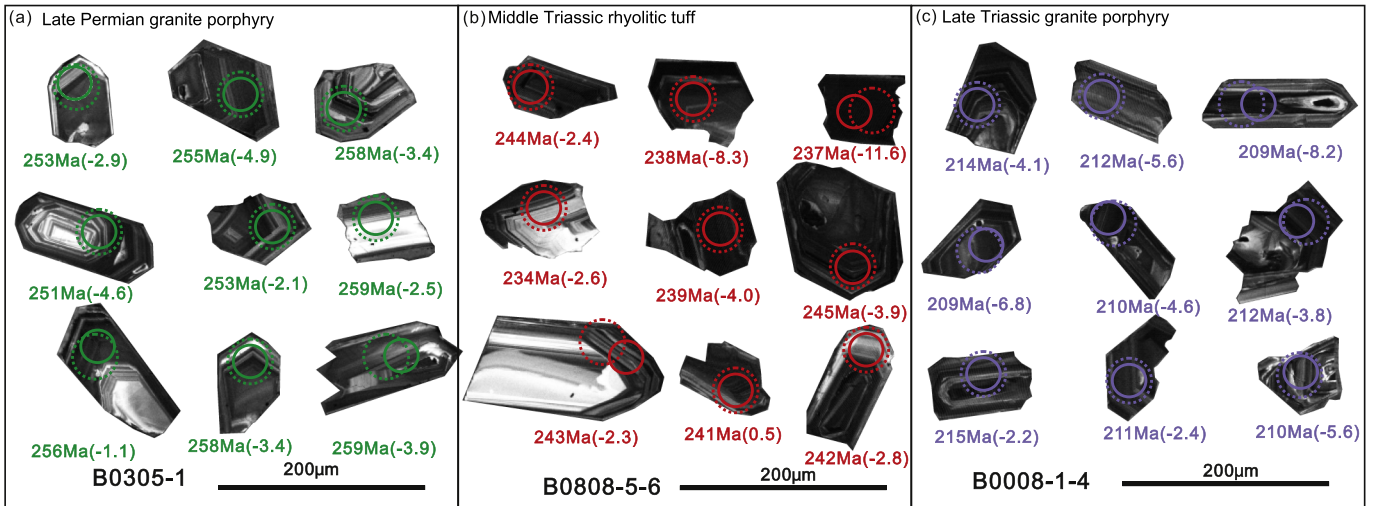


Fig. 5. Representative cathodoluminescence images of zircon grains with location of U-Pb (solid circle) and Hf (dotted circle) isotopic analysis for (a) Late Permian granite porphyry, (b) Middle Triassic rhyolitic tuff and (c) Late Triassic granite porphyry. The numbers before the brackets are the U-Pb ages and within the brackets are the $\varepsilon_{\text{Hf}}(t)$ values.

(Hoskin and Schaltegger, 2003). Thirteen grains from this sample plot on the Concordia line and yield a weighted mean $^{206}\text{Pb}/^{238}\text{U}$ extrusive age of 211 ± 2 Ma (MSWD = 0.57, Fig. 6e–f).

4.2. Major and trace elements geochemistry

The whole-rock major and trace element compositions are presented in Table 2. The granite porphyries display relatively high LOI (loss on ignition) values, suggesting that they possibly underwent alteration after emplacement. Overall, only Ba and U contents from the granite porphyries are inconsistent and show linear correlation with LOI values (Figs. 8a and 9). Considering that the later formation of barites due to hydrothermal alteration is prevalent in the Kengdenongshe area (Xia, 2017), we infer that the Ba contents of these rocks were altered. However, the samples from the granite porphyries have consistent contents of other elements (e.g. Sr, K, and LREE) (Fig. 9), and these elements do not show a linear correlation with the LOI values (Fig. 8b,c). Therefore, except Ba and U, the other elements can be used to trace the petrogenesis and tectonic setting of the granite porphyries. As for the rhyolitic tuff, only the sample B0806-0-1 contains some altered minerals including sericite and chlorite and has inconsistent elemental and isotopic composition with other samples, indicating alteration effect. Other samples with low LOI values and consistent compositions can be used to evaluate the petrogenesis and tectonic setting.

The Late Permian granite porphyry shows relatively more variable SiO₂ (69.3–76.3 wt%), Al₂O₃ (10.80–13.00 wt%), lower MgO (1.95–3.12 wt%) and higher K₂O (5.70–7.70 wt%) contents than the Late Triassic granite porphyry (SiO₂ = 72.9–75.9 wt%, Al₂O₃ = 11.05–11.80 wt%, MgO = 2.76–4.89 wt%, K₂O = 3.07–6.81 wt%). Both of the rocks show low CaO (<0.20 wt%) and Na₂O contents (<1.10 wt%) and high A/CNK ratios (1.40–3.03), which are characteristic of S-type granites (Fig. 7). The major oxides show negative correlations with SiO₂ (Fig. 8), indicating fractional crystallization during magma evolution. The granite porphyries show enrichment of the incompatible elements (e.g., Rb, Th, and U) and depletion of high field strength elements (HFSE: e.g., Nb, Ta, and Ti) (Fig. 9). They exhibit moderate light rare earth element (LREE) enrichment relative to heavy rare earth element (HREE), and a negative Eu anomaly, with (La/Yb)_N ratios of 8.48–11.19 and Eu/Eu* values of 0.24–0.36. The trace element geochemistry also indicates an upper continental crust (UCC) affinity (Fig. 9).

The rhyolitic tuff shows high SiO₂ contents, variable Al₂O₃ and K₂O contents, and low MgO, Na₂O and CaO contents, and A/CNK ratios of 1.06–2.86. It is also characterized by the enrichment of incompatible

elements (Rb, Ba, Th, and U) and the depletion of HFSE (Nb, Ta, P, and Ti) (Fig. 9). The (La/Yb)_N ratios of 5.86–20.06 and Eu/Eu* of 0.39–0.77 indicate LREE enrichment and the presence of a negative Eu anomaly. These geochemical features are similar to those of the granite porphyries and indicate a UCC affinity.

4.3. Whole-rock Sr and Nd isotopes

The Sr—Nd isotopic compositions of the granite porphyries and rhyolitic tuff are presented in Table 3 and Fig. 10a. The Late Permian granite porphyry has an $(^{87}\text{Sr}/^{86}\text{Sr})_i$ of 0.709918, ε_{Nd} (t) values of −6.0, and two-stage Nd model age, $T_{2\text{DM}}(\text{Nd})$, of 1.49 Ga. The rhyolitic tuff has variable Sr—Nd isotopic compositions with $(^{87}\text{Sr}/^{86}\text{Sr})_i$ ranging between 0.711666 and 0.720325, ε_{Nd} (t) ranging between −8.4 and −5.7, and $T_{2\text{DM}}(\text{Nd})$ between 1.31 and 1.84 Ga. The outlier sample in Fig. 10a is the altered sample B0806-0-1. The Late Triassic granite porphyry has a narrow range of $(^{87}\text{Sr}/^{86}\text{Sr})_i$ (0.718115–0.719052), ε_{Nd} (t) (−6.3 to −6.4), and $T_{2\text{DM}}(\text{Nd})$ (1.40–1.50 Ga).

4.4. Zircon Lu—Hf isotopes

The Lu—Hf isotopic data of zircons from the granite porphyries and rhyolitic tuff are illustrated in Table 4 and Fig. 10b–d. The Late Permian granite porphyry displays relatively homogeneous $^{166}\text{Hf}/^{177}\text{Hf}$ ratios of 0.282479 to 0.282605 and $\varepsilon_{\text{Hf}}(t)$ values from −4.9 to −0.1 with $T_{2\text{DM}}(\text{Hf})$ values from 1.61–1.95 Ga. The rhyolitic tuff has variable $^{166}\text{Hf}/^{177}\text{Hf}$ ratios of 0.282304 to 0.282662, $\varepsilon_{\text{Hf}}(t)$ values from −11.6 to +0.5 and $T_{2\text{DM}}(\text{Hf})$ values from 1.03–1.73 Ga. The Late Triassic granite porphyry displays $^{166}\text{Hf}/^{177}\text{Hf}$ ratios of 0.282424 to 0.282776 and $\varepsilon_{\text{Hf}}(t)$ values of −12.3 to +0.1, and has an ancient $T_{2\text{DM}}(\text{Hf})$ values ranging between 1.67 and 2.17 Ga.

5. Discussion

5.1. Rock classification

Granitic rocks are generally divided into A-, M-I-, and S- types according to their petrographic and geochemical characteristics (Chappell, 1999). The Kengdenongshe granite porphyries and rhyolitic tuff are characterized by the absence of alkali mafic minerals, low FeO^T, and high Ba contents (Fig. 9), and are therefore not A-type granites (Bonin, 2007; Jia et al., 2009). They display enriched Nd—Hf isotopic compositions, high SiO₂ contents (>69.0 wt%), which excludes them to

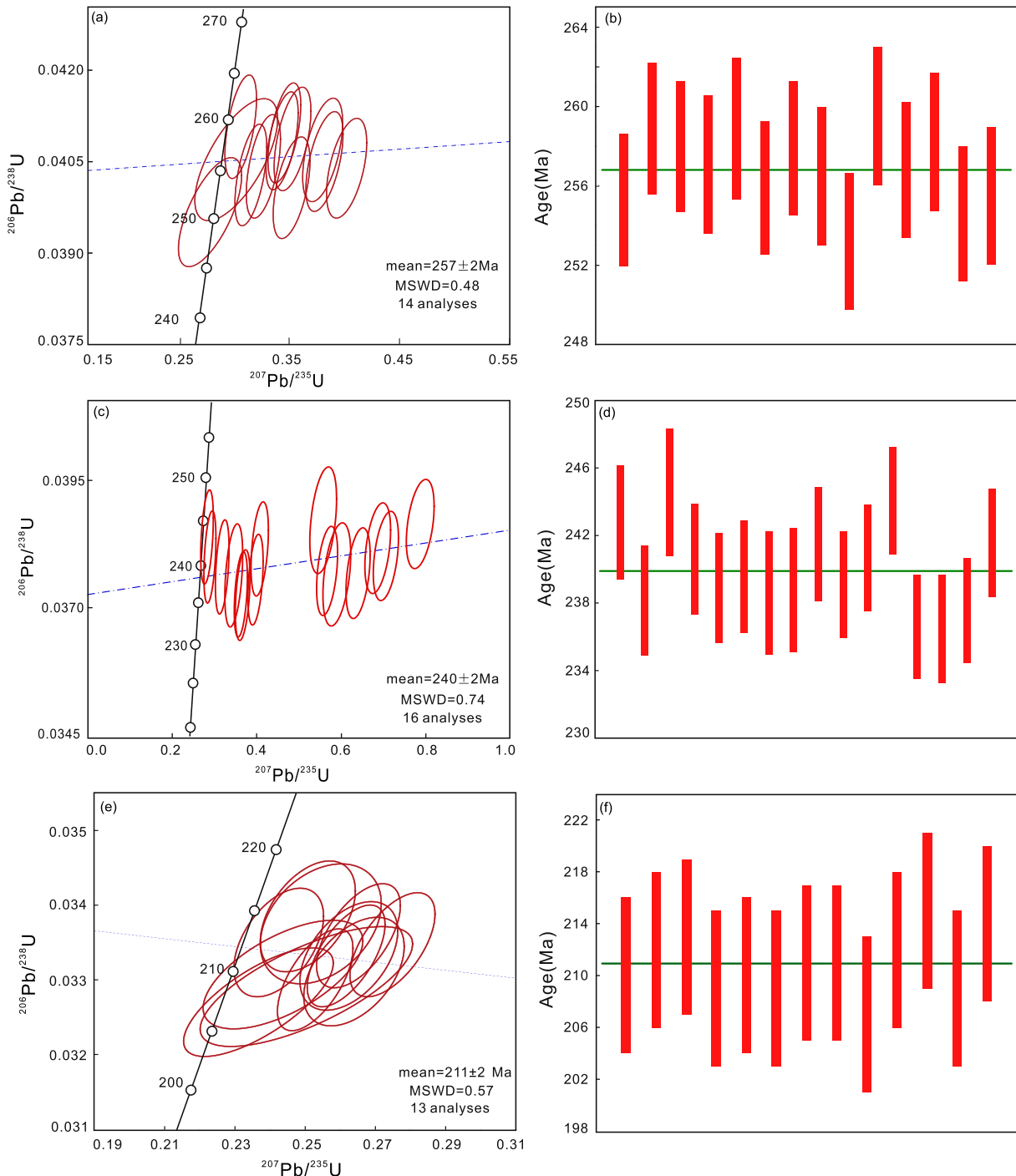


Fig. 6. Zircon U–Pb Concordia plots and bar charts for (a) Late Permian granite porphyry, (b) Middle Triassic rhyolitic tuff and (c) Late Triassic granite porphyry.

be classified as mantle-derived M-type granites (Whalen, 1985) that typically show low SiO_2 contents and depleted isotopic compositions (Collins et al., 1982; Pitcher, 1983).

The late Permian to late Triassic granite porphyries and rhyolitic tuff show high SiO_2 contents and A/CNK ratios of 1.06–3.03. These geochemical features indicate their high silica and peraluminous nature (Fig. 7a,b), which are similar to those of S-type granites or highly fractionated I-type granites (Chappell, 1999; Clemens, 2003). The evolution of the granite porphyries and rhyolitic tuff via fractional crystallization of feldspar and plagioclase is supported by the Harker diagrams in which SiO_2 shows a negative correlation with both Al_2O_3 and K_2O (Fig. 8d,e),

and strong negative Eu anomaly. The relationships between Rb and Sr, and the Y/Sr and Rb/Sr ratios (Fig. 11a,b) also indicate fractional crystallization of K-feldspar and plagioclase. The granite porphyries exhibit a negative correlation between SiO_2 and MgO , FeO^T and TiO_2 (Fig. 8g–i), further suggesting fractional crystallization of ferromagnesian minerals and Fe–Ti oxides. Although fractional crystallization occurred during magmatic evolution, the formation of these rocks is mainly controlled by partial melting, as suggested by the positive correlation between La and the La/Sm ratio (Fig. 11c). The samples have relatively high Zr and Zr/Hf ratio values, which are different from those of highly fractionated I-type granites, and they occur in the field of unfractionated granites in

Table 2

Major elements (wt%) and trace elements (ppm) data of samples from Kengdenongshe granite porphyries and rhyolitic tuff.

Samples	B0303-0-2	B0305-1	B0305-2	B0305-3	B0305-4	B0806-0-1	B0806-4-1	B0806-26-5	B0806-28-1	B0806-29-2
Late Permian granite porphyry						Rhyolitic tuff				
SiO ₂	76.3	69.3	72.5	70.0	74.6	77.2	80.7	83.1	80.4	79.4
TiO ₂	0.08	0.10	0.09	0.10	0.09	0.16	0.05	0.07	0.07	0.07
Al ₂ O ₃	10.80	12.45	13.00	12.33	12.09	12.75	9.89	8.20	8.98	8.44
Fe ₂ O ₃	0.88	1.20	0.73	1.19	0.92	1.96	0.43	0.25	0.45	0.09
MgO	1.95	3.12	2.30	3.09	2.57	0.58	0.57	0.83	1.11	0.12
CaO	0.05	0.06	0.20	0.06	0.12	0.05	0.02	0.22	0.30	0.18
Na ₂ O	0.57	0.31	1.08	0.31	0.66	0.24	0.09	0.06	0.03	0.13
K ₂ O	5.70	7.70	6.29	7.62	6.65	4.63	5.22	3.45	3.02	7.01
P ₂ O ₅	0.02	0.02	0.02	0.02	0.02	0.01	0.01	0.02	0.01	0.01
LOI	2.80	4.27	3.45	4.23	2.67	2.19	1.55	1.82	2.38	0.92
A/NK	1.52	1.40	1.51	1.40	1.46	2.35	1.70	2.13	2.70	1.08
A/CNK	1.51	1.40	1.48	1.40	1.44	2.33	1.70	2.03	2.49	1.06
Sc	9.73	13.30	12.30	13.17	12.16	8.18	8.60	5.49	6.79	10.40
V	6.73	15.70	10.40	15.54	12.40	20.70	7.98	84.70	138.00	5.34
Cr	5.52	4.49	6.52	4.45	5.23	13.00	6.89	7.58	5.19	8.65
Co	234	154	169	152	153	71	179	299	118	486
Ni	92.8	64.9	66.3	64.3	62.3	31.8	86.4	143.0	44.1	202.0
Ga	22.7	31.0	28.4	30.7	28.2	32.1	22.7	24.2	24.9	13.0
Rb	15.5	22.8	24.3	22.6	22.4	23.7	14.0	5.6	14.1	3.1
Sr	63	84	148	83	110	39	98	295	457	434
Y	50	51	46	50	46	44	32.7	35.1	36.8	30.8
Zr	167	193	196	191	185	290	141	155	148	136
Nb	15.5	22.8	24.3	22.6	22.4	23.7	14.0	5.6	14.1	3.1
Ba	6950	12,400	10,700	12,276	10,973	2210	19,500	14,700	40,600	34,900
La	58.3	70.3	73.7	69.6	68.4	101.0	39.3	52.6	55.7	51.1
Ce	95	115	123	114	113	173	66	87	91	85
Pr	10.20	12.30	13.00	12.18	12.02	17.70	7.27	9.27	9.74	8.79
Sm	6.42	7.50	7.60	7.43	7.17	9.63	5.30	5.44	6.08	5.25
Nd	33.5	40.0	41.8	39.6	38.9	55.7	25.4	29.9	32.3	28.4
Eu	0.76	0.68	0.59	0.68	0.60	1.80	0.71	1.12	1.39	1.28
Gd	6.27	7.32	6.89	7.24	6.75	8.09	4.77	5.19	7.19	4.78
Tb	1.10	1.18	1.13	1.17	1.10	1.27	0.80	0.79	0.88	0.75
Dy	6.90	7.53	6.74	7.45	6.78	6.96	5.00	4.82	5.23	4.57
Ho	1.50	1.62	1.45	1.60	1.46	1.43	1.09	1.05	1.12	0.95
Er	4.54	4.92	4.60	4.87	4.52	4.38	3.47	3.32	3.43	2.84
Tm	0.71	0.79	0.72	0.78	0.72	0.68	0.57	0.52	0.56	0.44
Yb	4.93	5.54	5.05	5.48	5.03	4.80	4.11	3.73	3.80	2.93
Lu	0.77	0.88	0.79	0.87	0.79	0.75	0.65	0.59	0.58	0.43
Hf	5.53	6.45	6.62	6.39	6.21	8.43	5.52	4.67	4.68	4.10
Ta	3.7	4.0	4.1	3.9	3.9	2.9	3.6	3.8	2.1	4.2
Pb	126	56	87	56	68	59	290	49	62	48
Th	31.5	37.8	40.8	37.4	37.3	53.5	26.9	23.1	25.8	20.3
U	12.1	7.3	7.1	7.2	6.8	10.8	7.9	5.7	4.6	11.7
(La/Yb) _N	8.48	9.10	10.47	9.10	9.75	15.09	6.86	10.12	10.51	12.51
Eu/Eu*	0.36	0.28	0.24	0.28	0.26	0.61	0.42	0.64	0.64	0.77
Samples	B0806-29-3	B0808-5-6	B0303-8-1	B0303-11-1	B0008-1-2	B0008-1-3	B0008-1-4	B0008-1-5	B0008-1-6	
Rhyolitic tuff						Late Triassic granite porphyry				
SiO ₂	76.6	82.0	90.1	83.4	72.9	75.9	72.9	74.8	74.4	
TiO ₂	0.08	0.04	0.08	0.13	0.09	0.08	0.09	0.09	0.09	
Al ₂ O ₃	12.00	8.39	4.40	7.00	11.80	11.05	11.80	11.48	11.43	
Fe ₂ O ₃	0.44	0.53	0.27	0.30	1.55	0.91	1.03	1.24	0.97	
MgO	0.88	1.82	0.50	0.91	4.89	2.76	2.98	3.84	2.87	
CaO	0.14	0.10	0.01	0.01	0.04	0.09	0.19	0.07	0.14	
Na ₂ O	0.10	0.13	0.02	0.07	0.32	0.27	0.24	0.30	0.26	
K ₂ O	7.19	4.24	1.38	2.10	3.07	5.14	6.81	4.13	5.43	
P ₂ O ₅	0.02	0.01	0.01	0.03	0.02	0.02	0.02	0.02	0.02	
LOI	1.56	2.12	1.43	2.96	5.24	2.73	3.33	4.00	3.03	
A/NK	1.51	1.74	2.88	2.92	3.06	1.84	1.52	2.31	1.81	
A/CNK	1.48	1.71	2.86	2.41	3.03	1.81	1.48	2.29	1.77	
Sc	12.10	6.23	4.56	6.24	5.83	6.95	11.90	6.42	9.43	
V	11.60	4.83	20.70	22.40	15.30	12.70	8.38	14.07	10.54	
Cr	8.66	6.35	9.14	8.76	9.59	5.44	14.30	7.55	9.87	
Co	240	249	391	350	124	136	190	131	163	
Ni	116.0	117.0	155.0	135.0	49.1	55.6	97.4	52.6	76.5	
Ga	23.2	17.6	16.6	11.7	35.2	26.5	20.5	31.0	23.5	
Rb	18.0	11.9	0.7	2.4	20.7	19.8	17.7	20.4	18.8	
Sr	158	48	352	562	27	52	80	39	66	
Y	48.5	46.5	34	34.2	44	37	42	41	39	
Zr	177	105	113	156	163	168	171	166	170	
Nb	18.0	11.9	0.7	2.4	20.7	19.8	17.7	20.4	18.8	
Ba	13,900	6310	21,100	27,400	715	8490	16,400	4626	12,446	

(continued on next page)

Table 2 (continued)

Samples	B0806-29-3	B0808-5-6	B0303-8-1	B0303-11-1	B0008-1-2	B0008-1-3	B0008-1-4	B0008-1-5	B0008-1-6
Rhyolitic tuff					Late Triassic granite porphyry				
La	66.6	39.4	28.1	46.7	60.3	64.4	61.4	62.7	62.9
Ce	111	71	43	72	104	107	105	106	106
Pr	11.80	7.70	4.34	7.62	10.90	11.50	11.40	11.26	11.45
Sm	7.33	6.06	2.51	4.18	6.17	6.83	7.20	6.53	7.02
Nd	37.8	26.7	14.1	24.3	34.2	36.7	37.0	35.6	36.9
Eu	0.99	0.79	0.65	0.73	0.60	0.70	0.70	0.66	0.70
Gd	6.75	6.15	2.83	4.43	5.83	6.34	7.14	6.12	6.74
Tb	1.15	1.08	0.37	0.48	0.99	1.00	1.12	1.00	1.06
Dy	7.07	6.87	2.18	2.42	6.10	5.80	6.82	5.98	6.31
Ho	1.50	1.48	0.46	0.51	1.35	1.26	1.44	1.31	1.35
Er	4.49	4.43	1.41	1.57	4.23	3.87	4.40	4.07	4.14
Tm	0.70	0.70	0.23	0.24	0.68	0.61	0.67	0.65	0.64
Yb	4.94	4.82	1.57	1.67	4.68	4.13	4.66	4.43	4.40
Lu	0.76	0.73	0.24	0.27	0.72	0.65	0.73	0.69	0.69
Hf	5.84	4.23	3.11	4.03	5.16	5.42	5.71	5.32	5.57
Ta	4.5	3.4	1.5	3.2	2.9	3.1	2.9	3.0	3.0
Pb	118	192	918	138	395	368	46	383	207
Th	34.1	22.4	10.1	14.9	30.5	33.0	32.5	31.9	32.8
U	6.0	6.0	3.4	2.5	10.4	4.9	5.9	7.7	5.4
(La/Yb) _N	9.67	5.86	12.84	20.06	9.24	11.19	9.45	10.15	10.27
Eu/Eu*	0.42	0.39	0.75	0.51	0.30	0.32	0.30	0.31	0.31

LOI = loss of ignition, A/NK = Al/Na + K in atomic ratio, A/CNK = Al/Ca + Na + K in atomic ratio. The La and Yb contents of chondrite used to calculate (La/Yb)_N are from Sun and McDonough (1989).

Fig. 11d. Thus, these granitic rocks can be classified as S-type rather than highly fractionated I-type granites. The occurrence of muscovite and the absence of amphibole as an accessory mineral is also typical of S-type granites (e.g., Jiao et al., 2015). The La vs SiO₂ and Y vs Rb diagrams (Fig. 7c,d) confirm the S-type affinity of the granite porphyries and rhyolitic tuff.

5.2. Tectonic evolution of the EKO from back-arc extension to continental collision and Post-collision

The EKO is linked to the evolution of the Paleo-Tethys Ocean and subsequent continental collision during the Permian and Triassic. As mentioned above, the model based on studies of regional I-type granitic

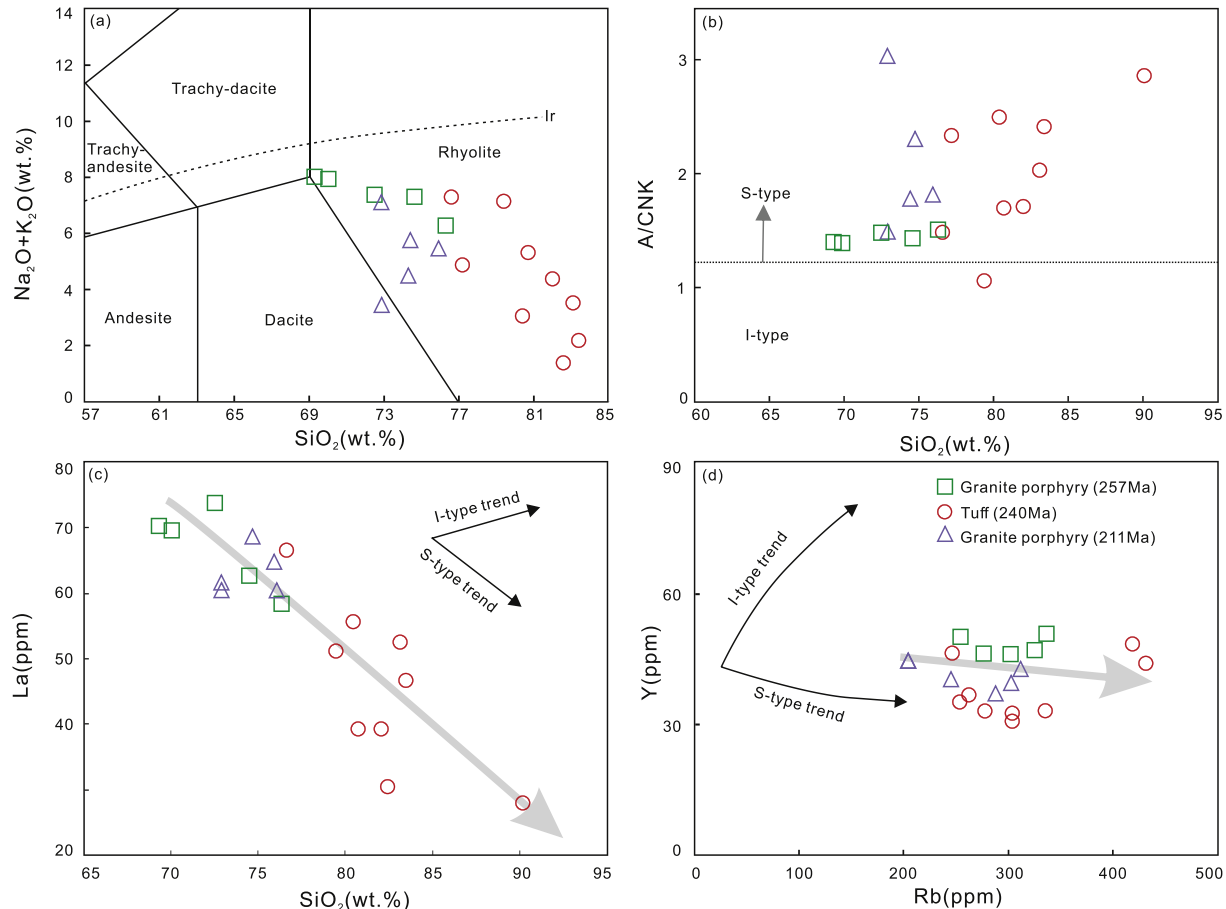


Fig. 7. (a) Na₂O + K₂O vs SiO₂ diagram (after Middlemost, 1994); (b) A/CNK vs SiO₂ diagram; (c) La vs SiO₂ diagram, and (d) Y vs Rb diagram for the Late Permian granite porphyry, Middle Triassic rhyolitic tuff, and Late Triassic granite porphyry.

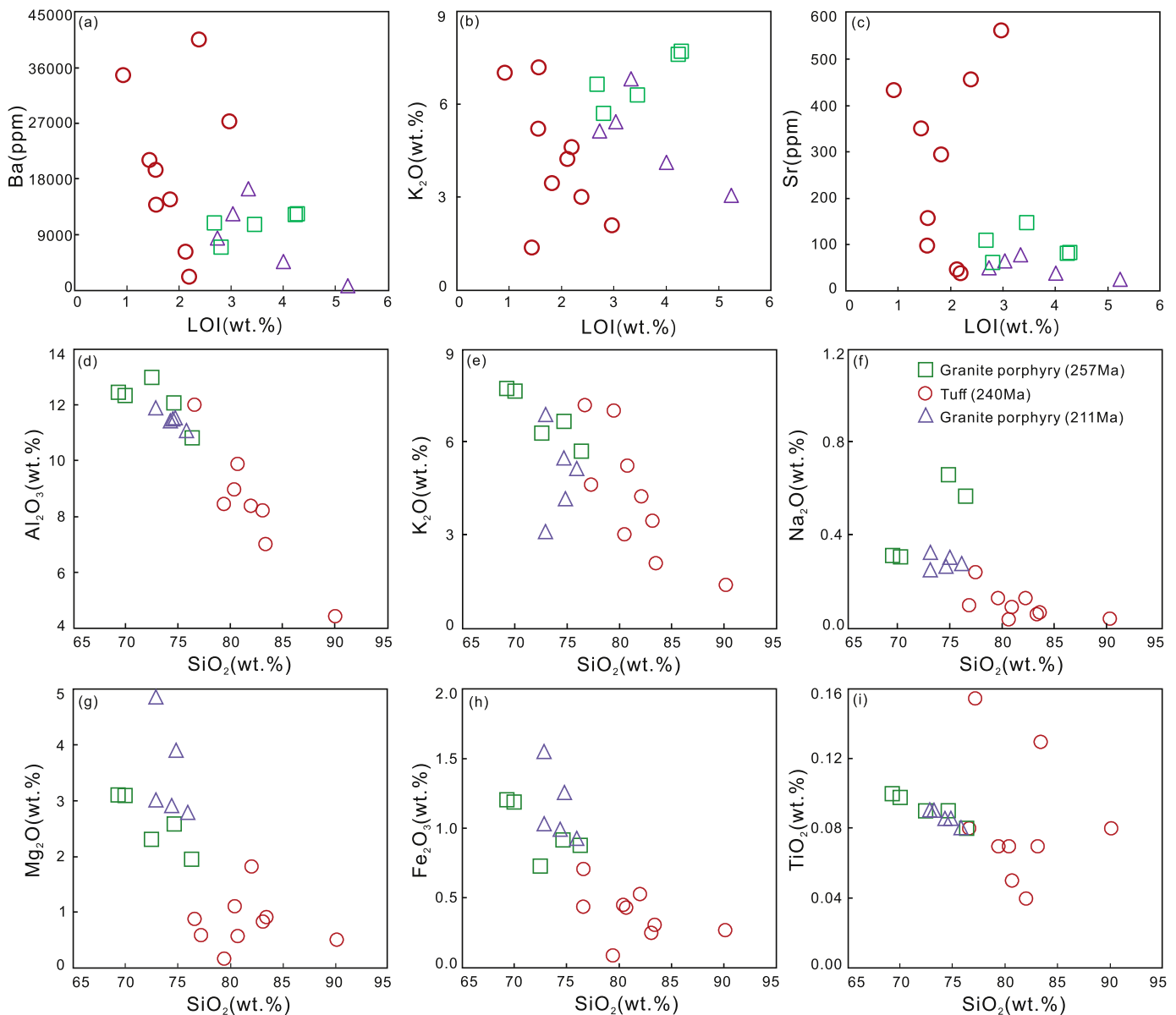


Fig. 8. Selected oxide plot for the Late Permian granite porphyry, Middle Triassic rhyolitic tuff, and Late Triassic granite porphyry.

rocks, which envisages single subduction of the Palo-Tethys Ocean from Late Permian to Early Triassic, is inconsistent with the distribution of regional mafic intrusions and sedimentary rocks, and lacks evidence from the studies on regional S-type granites. Therefore, we revised the tectonic evolution of the East Kunlun Orogen during Late Permian to Late Triassic in combination with regional granitic rocks, mafic intrusions, sedimentary units, structure, and crust maturity.

The petrographic observations and geochemical characteristics of the 257 Ma granite porphyry, 240 Ma rhyolitic tuff, and 211 Ma granite porphyry, suggest that they belong to S-type granitic rocks, which are typically considered to form during continental collision or in a post-collision setting (e.g., Barbarin, 1999; Liu and Zhao, 2018; Sylvester, 1998; Vernon, 1984; Wang et al., 2018; Zhu et al., 2018). Moreover, the S-type rocks are also used to constrain the back-arc extensional settings in subduction zones (e.g. Collins and Richards, 2008; Zhu et al., 2018).

The 257 Ma granite porphyry has relatively high Zr + Nb + Ce + Y contents (Fig. 11d). This geochemical feature is similar to the granitic rocks forming in an extension setting (Whalen et al., 1987) and thus

suggesting that the 257 Ma granite porphyry may also have been generated in an extension setting. Nearby the Kengdenongshe area, the Late Permian mafic rocks (266–262 Ma, Kong et al., 2017; Zhao et al., 2019), which were derived from partial melting of upwelling asthenosphere, show a geochemical affinity with back-arc basin basalt, suggesting Late Permian back-arc extension. Furthermore, the Kengdenongshe area is located north of numerous arc magmatic rock occurrences (situated between the SEKS and CEKS, Xiong, 2014), which indicate that the Late Permian S-type granite and mafic rocks were generated within a back-arc area.

Regional Late Permian to Middle Triassic (266–242 Ma) basic magmatic rocks (Fig. 1c) display a tholeiite to calc-alkaline geochemical signature while the tectonic settings changes from back-arc basin to continental arc (Zhao et al., 2019). The granitic intrusions can be classified with the 255–240 Ma calc-alkaline granite and granodiorite, which are considered to have been formed by mixing of slab-derived felsic magma and subcontinental mantle-derived mafic magma during oceanic subduction (Dong et al., 2018; Xiong et al., 2014), and 240–225 Ma high-K calc-alkaline granitic rocks which were sourced

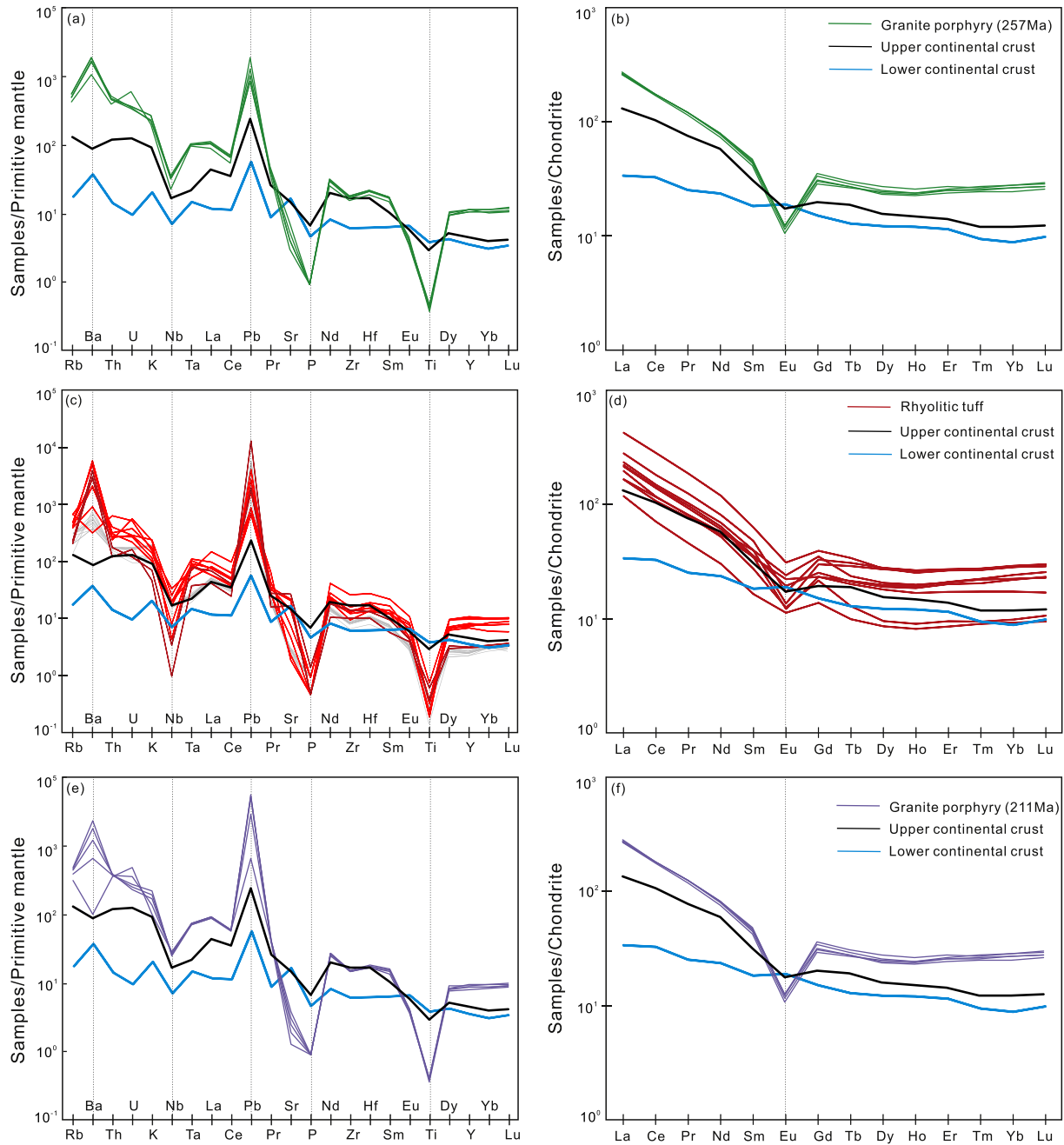


Fig. 9. Normalized trace element diagrams for the Late Permian granite porphyry, Middle Triassic rhyolitic tuff, and Late Triassic granite porphyry. Primitive mantle and chondrite values are from Sun and McDonough (1989), upper continental crust (UCC) and lower continental crust (LCC) values are from Rudnick and Gao (2003).

from oceanic-slab melting or melting of a thickened lower continental crust associated with continental collision (Song et al., 2013; Wang et al., 2009). The change from Early Triassic medium-K calc-alkaline to Middle and Late Triassic high-K calc-alkaline magmatism reflects the changes of crustal maturity during the transition from oceanic subduction to continental collision in the Middle Triassic (Deng et al., 2015). Furthermore, the transformation from open to tight folding during the Middle Triassic is consistent with the transformation from oceanic subduction to continental collision (Li, 2012). The unconformable contact between Early to Middle Triassic marine Xilikete Formation sedimentary and Middle to Late Triassic lake facies Babaoshan Formation suggests that the ocean had disappeared before the sedimentation of the Middle Triassic Babaoshan Formation (Chen et al., 2017). Therefore, the Middle Triassic S-type rhyolitic tuff should have been generated in a collisional setting.

The Late Triassic granite porphyry has similar geochemical features as the Late Permian granite porphyry with high $Zr + Nb + Ce + Y$ values, which suggests that it may also have been generated in an extensional setting including a back-arc basin and post-collisional setting. In the EKO, the Late Triassic mafic rocks (216 Ma, Fig. 1c) are considered to be derived from partial melting of a mixed mantle source composed of enriched lithospheric mantle and MORB-type asthenospheric mantle (Liu et al., 2017), and are associated with post-collisional extension and related orogenic collapse (Hu et al., 2016). The occurrence of regional Late Triassic A-type granites (Ding et al., 2011; Hu et al., 2016; Yu et al., 2015) also indicates Late Triassic post-collisional extension. Furthermore, the materials derived from upwelling asthenosphere and delaminated lithosphere contributed to the generation of regional Late Triassic granitic rocks (Hu et al., 2016; Luo et al., 2014; Yu et al., 2015), confirming asthenosphere upwelling in a Late Triassic post-

Table 3

Sr–Nd isotopic compositions of samples from the Kengdenongshe granite porphyries and rhyolitic tuff.

Number	Samples	Age(Ma)	$^{87}\text{Rb}/^{86}\text{Sr}$	$^{87}\text{Sr}/^{86}\text{Sr}$	$\pm 2\sigma$	$(^{87}\text{Sr}/^{86}\text{Sr})_i$	$^{147}\text{Sm}/^{144}\text{Nd}$	$^{143}\text{Nd}/^{144}\text{Nd}$	$\pm 2\sigma$	$\varepsilon_{\text{Nd}}(t)$	$T_{\text{DM}}(\text{Ga})$	$T_{\text{DM}}(\text{Ga})$
B0303-0-2	granite porphyry	257	11.68	0.75250	0.00004	0.709918	0.115847	0.512195	0.000012	-6.0	1.51	1.49
B0303-11-1	rhyolitic tuff	240	0.75	0.71439	0.00006	0.103983	0.512203	0.000008	-5.5	1.47	1.32	
B0806-0-1	rhyolitic tuff	240	32.36	0.83070	0.00004	0.720325	0.104508	0.512049	0.000012	-8.7	1.72	1.54
B0806-4-1	rhyolitic tuff	240	8.94	0.74218	0.00004	0.711689	0.126135	0.512208	0.000012	-6.2	1.52	1.64
B0806-28-1	rhyolitic tuff	240	1.66	0.71748	0.00004	0.711817	0.113787	0.512190	0.000008	-6.2	1.52	1.47
B0806-29-3	rhyolitic tuff	240	7.68	0.73903	0.00006	0.712842	0.117221	0.512189	0.000016	-6.3	1.53	1.52
B0808-5-6	rhyolitic tuff	240	15.04	0.76504	0.00006	0.713752	0.137201	0.512224	0.000010	-6.3	1.52	1.84
B0008-1-2	granite porphyry	211	22.11	0.78729	0.00006	0.720907	0.109057	0.512191	0.000010	-6.4	1.51	1.40
B0008-1-3	granite porphyry	211	16.22	0.76680	0.00006	0.718115	0.112499	0.512193	0.000010	-6.4	1.51	1.44
B0008-1-4	granite porphyry	211	11.31	0.75301	0.00006	0.719052	0.117632	0.512205	0.000010	-6.3	1.50	1.50

 $(^{87}\text{Sr}/^{86}\text{Sr})_i$ and $\varepsilon_{\text{Nd}}(t)$ values are calculated at $t = 266$ Ma based on present-day $(^{147}\text{Sm}/^{144}\text{Nd})_{\text{CHUR}} = 0.1967$ and $(^{143}\text{Nd}/^{144}\text{Nd})_{\text{CHUR}} = 0.512638$. T_{DM} values are calculated based on present-day $(^{147}\text{Sm}/^{144}\text{Nd})_{\text{DM}} = 0.2137$ and $(^{143}\text{Nd}/^{144}\text{Nd})_{\text{DM}} = 0.51315$. $\lambda_{\text{Rb}} = 1.42 \times 10^{-11} \text{ year}^{-1}$ (Steiger and Jäger, 1977), $\lambda_{\text{Sm}} = 6.54 \times 10^{-12} \text{ year}^{-1}$ (Lugmair and Marti, 1978).

collision extensional setting. Therefore, the 211 Ma granite porphyry was likely generated in a post-collision extensional setting.

In summary, the tectonic evolution of the EKO during Late Permian to Late Triassic involved five stages: (1) Initial subduction of the Paleo-Tethys Ocean commencing before 278 Ma; (2) Late Permian back-arc extension (Fig. 13a); (3) Late Permian to Early Triassic active subduction of the Paleo-Tethys Ocean (Fig. 13b); (4) Middle Triassic

continental collision (Fig. 13c); (5) Late Triassic post-collisional extensional setting (Fig. 13d).

5.3. Multi-stage melting of upper continental crust

It has been proposed that peraluminous melts can be produced by dehydration melting of metaluminous protoliths at low H_2O -activity

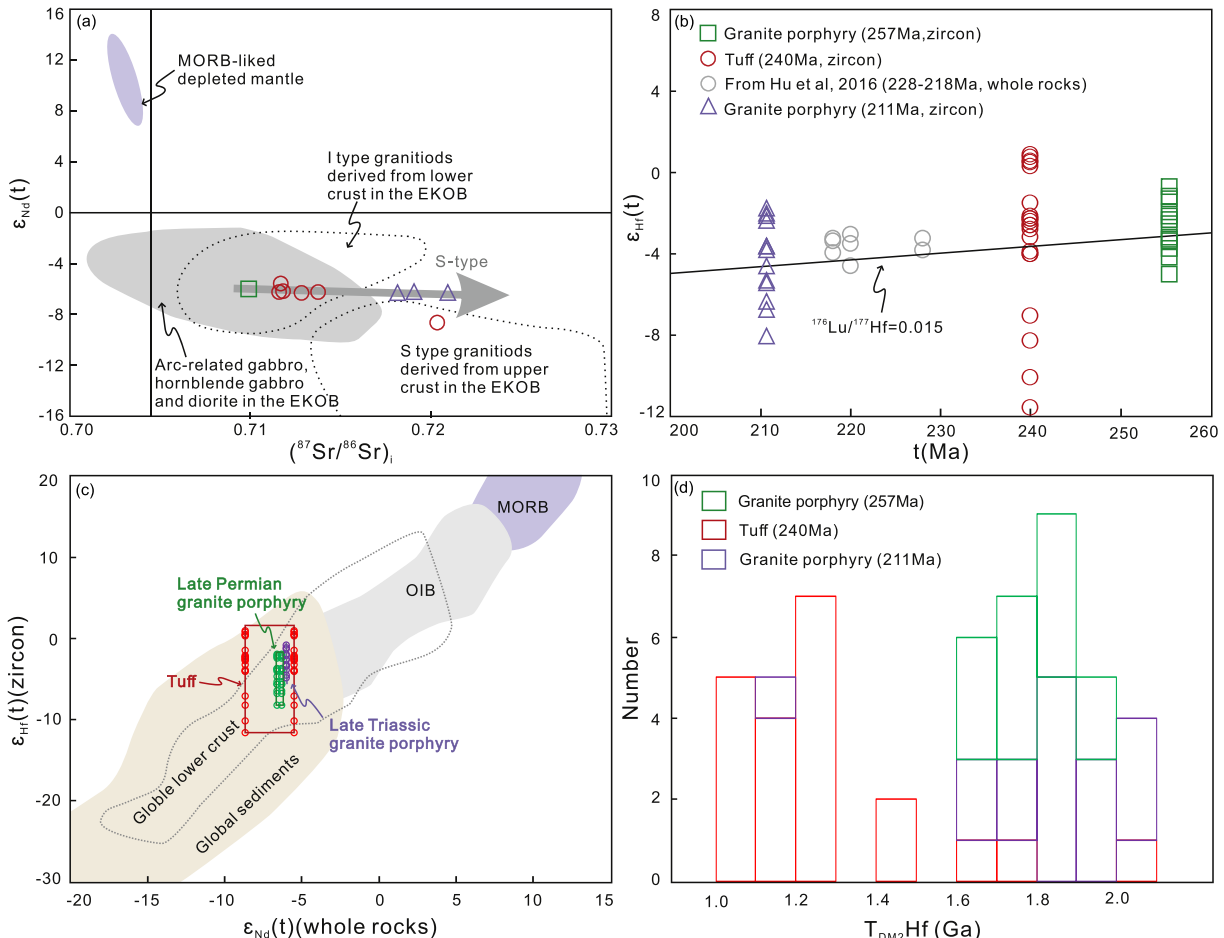


Fig. 10. (a) $\varepsilon_{\text{Nd}}(t)$ vs $(^{87}\text{Sr}/^{86}\text{Sr})$ plot; (b) zircon $\varepsilon_{\text{Hf}}(t)$ vs zircon U–Pb ages plot; (c) zircon $\varepsilon_{\text{Hf}}(t)$ vs whole-rock $\varepsilon_{\text{Nd}}(t)$ plot and (d) Histogram of $T_{\text{DM2}} \text{Hf}$ values for the Late Permian granite porphyry, Middle Triassic rhyolitic tuff and the Late Triassic granite porphyry. The field of depleted mantle is from Workman and Hark (2005); I-type granites derived from lower crust and S-type granites derived from upper crust in the EKO are from Xiong et al. (2014); arc-related magmatic rocks in the EKO are from Xiong et al. (2011), Li et al. (2012), Wang et al. (2014), and Zhao et al. (2018); (b) zircon $\varepsilon_{\text{Hf}}(t)$ vs zircon U–Pb ages plot; (c) zircon $\varepsilon_{\text{Hf}}(t)$ vs whole-rock $\varepsilon_{\text{Nd}}(t)$ plot, fields of OIB and MORB referenced from Kempton and McGill (2002), of global sediments referenced from Vervoort and Blichert-Toft (1999), of lower crust referenced from Dobosi et al. (2003). (d) Histogram of $T_{\text{DM2}} \text{Hf}$ values for the Late Permian granite porphyry, Middle Triassic rhyolitic tuff, and the Late Triassic granite porphyry.

Table 4

Hf isotopic data for zircons of sample B0305-1 from Late Permian granite porphyry, B0808-5-6 from rhyolitic tuff and B0008-1-4 from Late Triassic granite porphyry.

Number	$^{176}\text{Yb}/^{177}\text{Hf}$	$^{176}\text{Lu}/^{177}\text{Hf}$	$^{176}\text{Hf}/^{177}\text{Hf}$	2σ	$\epsilon_{\text{Hf}}(0)$	$\epsilon_{\text{Hf}}(t)$	2σ	$T_{\text{DM}}(\text{Hf})$ (Ga)	$T_{\text{DM2}}(\text{Hf})$ (Ga)	$F_{\text{Lu/Hf}}$
B0305-1 Late Permian granite porphyry										
1	0.035819	0.001445	0.282549	0.000022	-7.9	-2.5	1.3	1.01	1.75	-0.96
2	0.041447	0.001683	0.282566	0.000023	-7.3	-1.9	1.3	0.99	1.71	-0.95
3	0.024241	0.001006	0.282479	0.000021	-10.4	-4.9	1.3	1.09	1.95	-0.97
4	0.040920	0.001625	0.282523	0.000024	-8.8	-3.4	1.3	1.05	1.83	-0.95
5	0.066520	0.002523	0.282496	0.000031	-9.8	-4.6	1.5	1.11	1.92	-0.92
6	0.031841	0.001303	0.282524	0.000021	-8.8	-3.4	1.3	1.04	1.82	-0.96
7	0.071728	0.002820	0.282605	0.000022	-5.9	-0.7	1.3	0.96	1.61	-0.92
8	0.062539	0.002463	0.282564	0.000023	-7.3	-2.1	1.3	1.01	1.72	-0.93
9	0.053101	0.002193	0.282532	0.000020	-8.5	-3.2	1.2	1.05	1.81	-0.93
10	0.062295	0.002527	0.282514	0.000034	-9.1	-3.9	1.6	1.09	1.87	-0.92
11	0.030822	0.001263	0.282583	0.000022	-6.7	-1.3	1.3	0.95	1.65	-0.96
12	0.059658	0.002419	0.282554	0.000026	-7.7	-2.5	1.4	1.03	1.75	-0.93
13	0.030930	0.001175	0.282586	0.000024	-6.6	-1.1	1.3	0.95	1.64	-0.96
B0808-5-6 Rhyolitic tuff										
1	0.062656	0.002517	0.282567	0.000035	-7.3	-2.4	1.6	1.01	1.73	-0.92
2	0.033231	0.001408	0.282430	0.000023	-12.1	-7.0	1.3	1.17	1.43	-0.96
3	0.033143	0.001374	0.282396	0.000025	-13.3	-8.3	1.3	1.22	1.49	-0.96
4	0.058598	0.002256	0.282659	0.000045	-4.0	0.9	1.9	0.87	1.02	-0.93
5	0.056365	0.001998	0.282304	0.000035	-16.5	-11.6	1.6	1.37	1.66	-0.94
6	0.039011	0.001582	0.282589	0.000023	-6.5	-1.5	1.3	0.95	1.14	-0.95
7	0.090293	0.003588	0.282567	0.000039	-7.3	-2.6	1.7	1.04	1.20	-0.89
8	0.059116	0.002260	0.282520	0.000050	-8.9	-4.0	2.1	1.07	1.27	-0.93
9	0.059993	0.002486	0.282522	0.000026	-8.9	-4.0	1.4	1.08	1.27	-0.93
10	0.029455	0.001244	0.282343	0.000026	-15.2	-10.1	1.4	1.29	2.35	-0.96
11	0.044621	0.001826	0.282522	0.000023	-8.8	-3.9	1.3	1.06	1.26	-0.94
12	0.079953	0.003234	0.282654	0.000034	-4.2	0.6	1.6	0.90	1.04	-0.90
13	0.087949	0.003582	0.282662	0.000031	-3.9	0.8	1.5	0.90	1.03	-0.89
14	0.095329	0.003841	0.282655	0.000039	-4.2	0.5	1.7	0.91	1.04	-0.88
15	0.087725	0.003480	0.282575	0.000043	-7.0	-2.3	1.8	1.03	1.18	-0.90
16	0.057672	0.002259	0.282572	0.000042	-7.1	-2.2	1.8	1.00	1.18	-0.93
17	0.189491	0.006033	0.282560	0.000044	-7.5	-3.2	1.9	1.13	1.23	-0.82
18	0.034923	0.001486	0.282565	0.000021	-7.3	-2.3	1.3	0.98	1.18	-0.96
19	0.040683	0.001671	0.282552	0.000070	-7.8	-2.8	2.7	1.01	1.21	-0.95
20	0.108734	0.004147	0.282651	0.000039	-4.3	0.3	1.7	0.93	1.05	-0.88
21	0.045691	0.001861	0.282559	0.000042	-7.5	-2.6	1.8	1.00	1.20	-0.94
B0008-1-4 Late Triassic granite porphyry										
1	0.073406	0.002811	0.282536	0.000030	-8.4	-4.1	1.5	1.06	1.85	-0.92
2	0.108011	0.004240	0.282553	0.000036	-7.8	-3.7	1.6	1.08	1.82	-0.87
3	0.066379	0.002606	0.282542	0.000034	-8.1	-3.8	1.6	1.05	1.83	-0.92
4	0.065084	0.002621	0.282494	0.000044	-9.8	-5.6	1.9	1.12	1.97	-0.92
5	0.045926	0.001852	0.282456	0.000053	-11.2	-6.8	2.1	1.15	2.07	-0.94
6	0.090957	0.003579	0.282424	0.000043	-12.3	-8.2	1.8	1.26	2.17	-0.89
7	0.087661	0.003244	0.282472	0.000069	-10.6	-6.4	2.7	1.17	2.03	-0.90
8	0.115624	0.004135	0.282526	0.000032	-8.7	-4.6	1.5	1.12	1.89	-0.88
9	0.062763	0.002503	0.282544	0.000037	-8.1	-3.8	1.7	1.04	1.82	-0.92
10	0.085084	0.003368	0.282593	0.000049	-6.3	-2.2	2.0	0.99	1.69	-0.90
12	0.080057	0.003079	0.282591	0.000036	-6.4	-2.2	1.6	0.99	1.70	-0.91
12	0.068521	0.002769	0.282583	0.000048	-6.7	-2.4	2.0	0.99	1.71	-0.92
13	0.074960	0.002518	0.282493	0.000042	-9.8	-5.6	1.8	1.12	1.97	-0.92
14	0.051072	0.002075	0.282596	0.000045	-6.2	-1.9	1.9	0.96	1.67	-0.94
15	0.072784	0.002531	0.282499	0.000029	-9.7	-5.4	1.4	1.11	1.95	-0.92

The parameter used in our calculations: $(^{176}\text{Lu}/^{177}\text{Hf})_{\text{CHUR}} = 0.0332$, $(^{176}\text{Hf}/^{177}\text{Hf})_{\text{CHUR}} = 0.282772$ (Blichert-Toft and Albarède, 1997); $(^{176}\text{Lu}/^{177}\text{Hf})_{\text{DM}} = 0.0384$, $(^{176}\text{Hf}/^{177}\text{Hf})_{\text{DM}} = 0.28325$ (Griffin et al., 2000); $\lambda(^{176}\text{Lu}) = 1.867 \times 10^{-11} \text{ a}^{-1}$ (Söderlund et al., 2004). The $^{176}\text{Lu}/^{177}\text{Hf}$ (C) = 0.015 (Griffin et al., 2000).

conditions (Rapp and Watson, 1995; Sylvester, 1998) or by melting of metamorphic rocks in the UCC, including clay-rich metapelites, clay-poor metagreywackes and amphibolite (Petford and Atherton, 1996; Sylvester, 1998; Patino-Douce, 1998; Koester et al., 2002). The melts from dehydration melting of metaluminous protoliths usually have low $\text{K}_2\text{O}/\text{Na}_2\text{O}$ ratios and relatively high contents of mafic minerals (Sylvester, 1998), which is inconsistent with the Kengdenongshe granite porphyries and rhyolitic tuff that show high $\text{K}_2\text{O}/\text{Na}_2\text{O}$ (>9.6) mass ratios and minor contents of mafic minerals (only biotite).

We propose that clay-poor meta-sedimentary in the UCC were the main source for the granite porphyries and rhyolitic tuff. Evidence for this includes the following. (1) The granite porphyries and rhyolitic

tuff show high SiO_2 contents and high A/CNK ratios, and display similar geochemical features with the UCC (Fig. 9), indicative of melting of a UCC source. (2) The Nb/Th and Ta/U ratios are usually used to distinguish the magma sources as these elements have a similar partition coefficient and the ratios are hardly influenced by magma evolution. The porphyries and rhyolitic tuff all plot nearby the UCC on the $(\text{Ta}/\text{U})_{\text{PM}}$ vs $(\text{Nb}/\text{Th})_{\text{PM}}$ diagram (Fig. 12a). (3) They have low $(\text{Na}_2\text{O} + \text{K}_2\text{O})/(\text{MgO} + \text{TiO}_2 + \text{FeO}^{\text{T}})$ and $\text{Al}_2\text{O}_3/(\text{MgO} + \text{TiO}_2 + \text{FeO}^{\text{T}})$ mass ratios, indicative of the derivation from melting of clay-poor rocks (Fig. 12 b,c). (4) The felsic intrusions in the Kengdenongshe display low Rb/Ba and Rb/Sr , and high $\text{CaO}/\text{Na}_2\text{O}$ ratios. Peraluminous granites derived from plagioclase-rich, clay-poor meta-sedimentary usually have higher

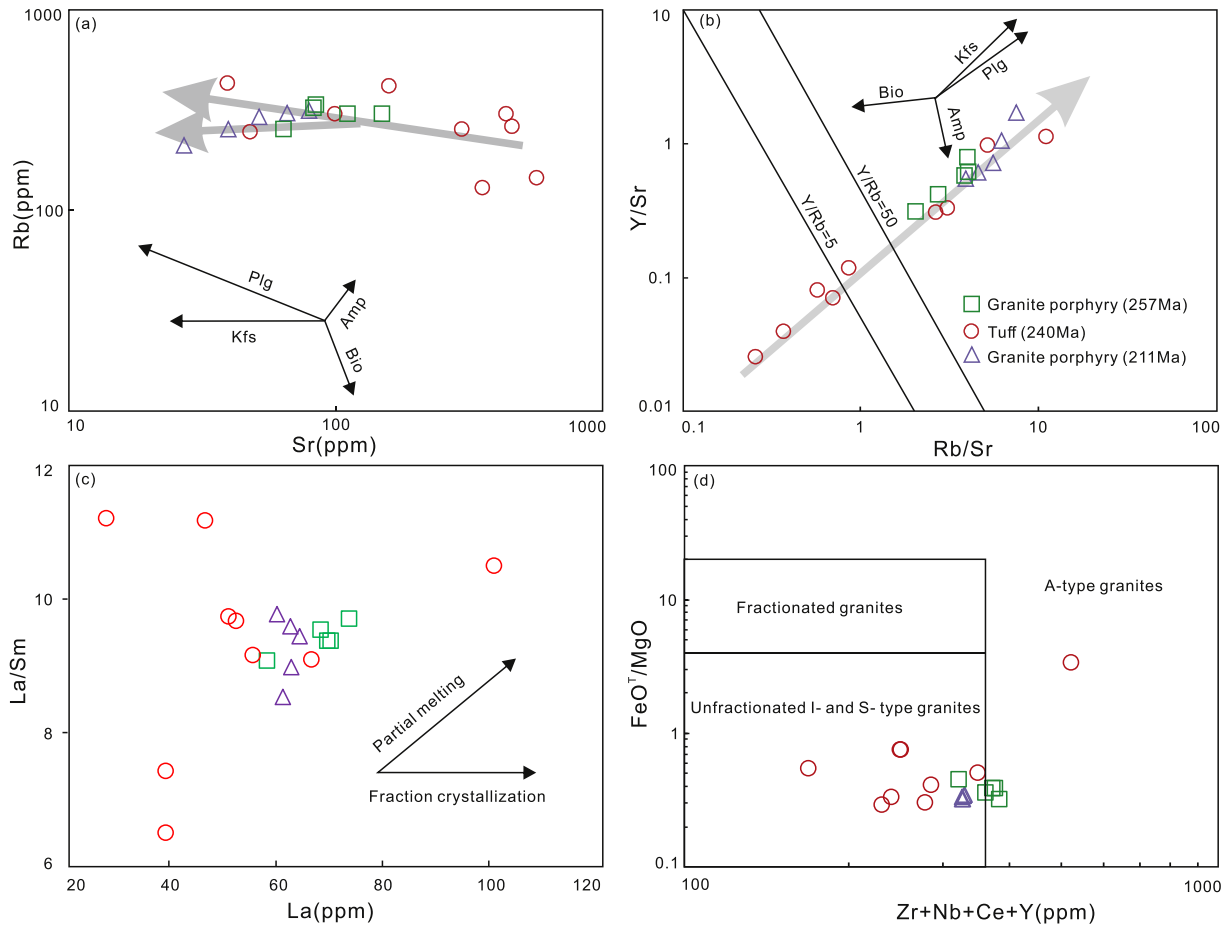


Fig. 11. (a) Rb vs Sr, (b) Y/Sr vs Rb/Sr, (c) La/Sm vs La, and (d) FeO^T/MgO vs $\text{Zr} + \text{Nb} + \text{Ce} + \text{Y}$ plot for Late Permian granite porphyry, Middle Triassic rhyolitic tuff, and Late Triassic granite porphyry.

$\text{CaO}/\text{Na}_2\text{O}$ (>0.3) ratios than those from clay-rich metapelites (<0.3) (Sylvester, 1998), as well as the lower Rb/Ba and Rb/Sr ratios (Janoušek et al., 2004). (5) The $\varepsilon_{\text{Nd}}(t)$ and $\varepsilon_{\text{Hf}}(t)$ values range between -8.4 to -5.7 and -12.3 to $+0.5$, respectively. These values overlap with those of global sediments (Vervoort and Blichert-Toft, 1999), suggesting that their parental magma was derived predominately from crustal meta-sedimentary rocks. (6) The corresponding two-stage Hf modal ages of the rhyolitic tuff and granite porphyries range between 1.03 and 1.73 Ga, and between 1.67 and 2.17 Ga, respectively, which are the same with regional basement of Paleoproterozoic Jinshui Group (2366–1600 Ma, Wang et al., 2007; Chen et al., 2006; Zhang et al., 2003) and Xiaomiao Formation (1600–1035 M, Chen et al., 2006; Jin et al., 2015; Wang et al., 2004). This implies a significant contribution of ancient continental crust to the formations of the Kengdenongshe granite porphyries and rhyolitic tuff.

It is suggested that the geochemical features of S-type granites may be influenced by peritectic entrainment, fluid-flux melting, magma mixing and source heterogeneity (e.g. Stevens et al., 2007; Villaros et al., 2012; Weinberg and Hasalová, 2015). Peritectic assemblage entrainment usually is the dominant mechanism for the compositional variations of garnet/cordierite-rich S-type granites (Gao et al., 2016), but these minerals are not found in this study. Furthermore, peritectic entrainment usually causes wide variations of major oxides (Stevens et al., 2007), which is also inconsistent with the features of the S-type granites in our study. The most significant feature of water-fluxed

melting is its capacity to produce voluminous melting (Weinberg and Hasalová, 2015), thus the source of the small-scale granite porphyries may not be water-rich. In most cases granitic magmas are produced by decompression melting or heat input during lithospheric extension and asthenosphere upwelling in the back-arc basin, not through hydrous fluxing (Bea, 2012; Collins et al., 2016). The melting of upper crustal regions in collision zones is also usually characterized by fluid-absent conditions (Powell, 1983; Thompson, 1983). Therefore, peritectic entrainment and fluid-flux melting are probably not responsible for the generation of these S-type granites.

Possible magma mixing or source heterogeneity is suggested by the positive correlations between FeO and MgO contents (Fig. 12). However, the small-scale rock masses do not have any enclaves and their compositions are consistent, i.e. they are unlikely to be the results of magma mixing. Although the rocks display a wide range of Hf isotopic values, the granitic rocks in the EKO related to magma mixing actually have more uniform isotopic compositions than the end members (e.g., Chen et al., 2017). Villaros et al. (2012) suggested that the variable zircon $\varepsilon_{\text{Hf}}(t)$ values of S-type granites are usually inherited from heterogeneous magma sources. The wide range of two-stage Hf model ages ($T_{2\text{DM}}$) (1.04–2.35 Ga) also indicates that crustal materials of different ages may have been involved in the genesis of these granites. Geochemically, the samples of the granitic porphyries and rhyolitic tuff overlap with meta-sediments and amphibolites (Fig. 12b,c) further suggesting a heterogeneous crustal source comprising clay-poor

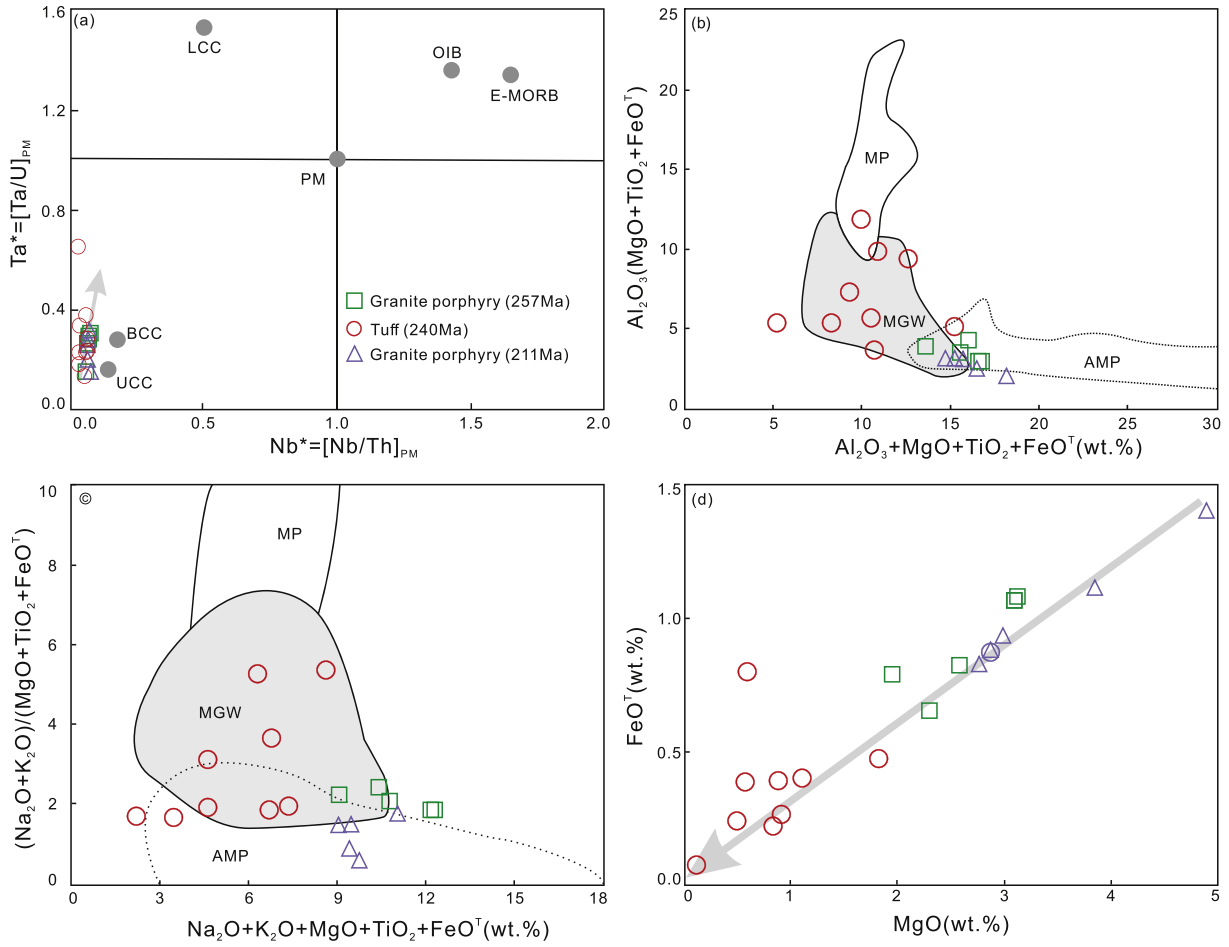


Fig. 12. (a) Primitive-mantle normalized plot of Ta/U vs Nb/Th (after Niu and Batiza, 1997). Data of primitive mantle and average oceanic basalts (OIB, E-MORB, N-MORB) are from Sun and McDonough (1989). Crust compositions (BCC, LCC, UCC) are from Rudnick and Gao (2003). (b,c) $\text{Al}_2\text{O}_3/(\text{FeO} + \text{MgO} + \text{TiO}_2)$ vs $\text{Al}_2\text{O}_3 + \text{FeO} + \text{MgO} + \text{TiO}_2$ and $(\text{Na}_2\text{O} + \text{K}_2\text{O})/(\text{FeO} + \text{MgO} + \text{TiO}_2)$ vs $\text{Na}_2\text{O} + \text{K}_2\text{O} + \text{MgO} + \text{TiO}_2 + \text{FeO}^\text{T}$ plots (fields of partial melting in felsic metapelites, metagreywackes, and amphibolite obtained from experimental studies; Douc, 1999). (d) FeO^T vs MgO plot. UCC: upper continental crust; BCC: bulk continental crust; LCC: lower continental crust; PM: primitive mantle; OIB: ocean island basalt; E-MORB: enriched middle oceanic ridge basalt; MP: metapelites; MGW: metagreywackes; AMP: amphibolite.

meta-sedimentary rocks and amphibolite, which both are included in the Proterozoic Xiaomiao Formation and Jinshui Group (Zhao et al., 2018).

The key factor for crustal melting and generation of S-type granites is anatexis after crustal thickening, or heat input through asthenospheric upwelling or mantle convection (Bea, 2012; Zhu et al., 2018). The Late Permian gabbro in the northern part of the Kengdenongshe area indicates that asthenospheric upwelling likely occurred during the Late Permian (Kong et al., 2017; Zhao et al., 2019). Asthenospheric upwelling in a back-arc basin can provide adequate heat for the melting of upper continental crust (Bea, 2012), resulting in the formation of the 257 Ma granite porphyry in the Kengdenongshe area (Fig. 13a). Asthenospheric upwelling in a back-arc basin has also been used to explain the generation of numerous S-type granites in the Circum-Pacific orogens (Collins and Richards, 2008). The Middle Triassic transformation of regional medium-K calc-alkaline to high-K calc-alkaline magmatism (Wang et al., 2009; Xiong, 2014) indicates Middle Triassic crustal thickening, as the medium-K calc-alkaline rocks relate to a crustal thickness of 17–40 km and the high-K calc-alkaline rocks relate to a crustal thickness >40 km (Deng et al., 2015). The meta-sedimentary successions buried during the crustal thickening in continent-continent collision were the most plausible source for the peraluminous S-type granite (Barbarin, 1999). Thus, the Middle Triassic rhyolitic tuff might be linked to anatexis during continental collision. In the Late Triassic,

asthenosphere upwelling was documented by the studies of regional mafic rocks and granitic rocks (Liu et al., 2017). Asthenospheric upwelling likely induced crustal melting and generated the Late Triassic S-type granitic rocks in a post-collisional setting (e.g., Sylvester, 1998; Fig. 13d).

6. Conclusions

- (1) S-type felsic igneous rocks in Kengdenongshe yield zircon U—Pb ages ranging from Late Permian (ca. 257 Ma) to Late Triassic (ca. 211 Ma).
- (2) The tectonic evolution of the EKO during the Late Permian to Late Triassic involved Late Permian back-arc extension, continuous Late Permian to Early Triassic subduction, Middle Triassic continental collision, and Late Triassic post-collisional extension.
- (3) The Kengdenongshe granite porphyries and rhyolitic tuff were formed from heterogeneous crustal sources including clay-poor meta-sedimentary rocks and amphibolite in the Paleoproterozoic Xiaomiao Formation and Jinshui Group basement.
- (4) The Late Permian and Late Triassic granite porphyries are associated with asthenospheric upwelling in back-arc basin and post-collision extensional settings, respectively. The Middle Triassic rhyolitic tuff formed during crustal thickening in the continental collision zone.

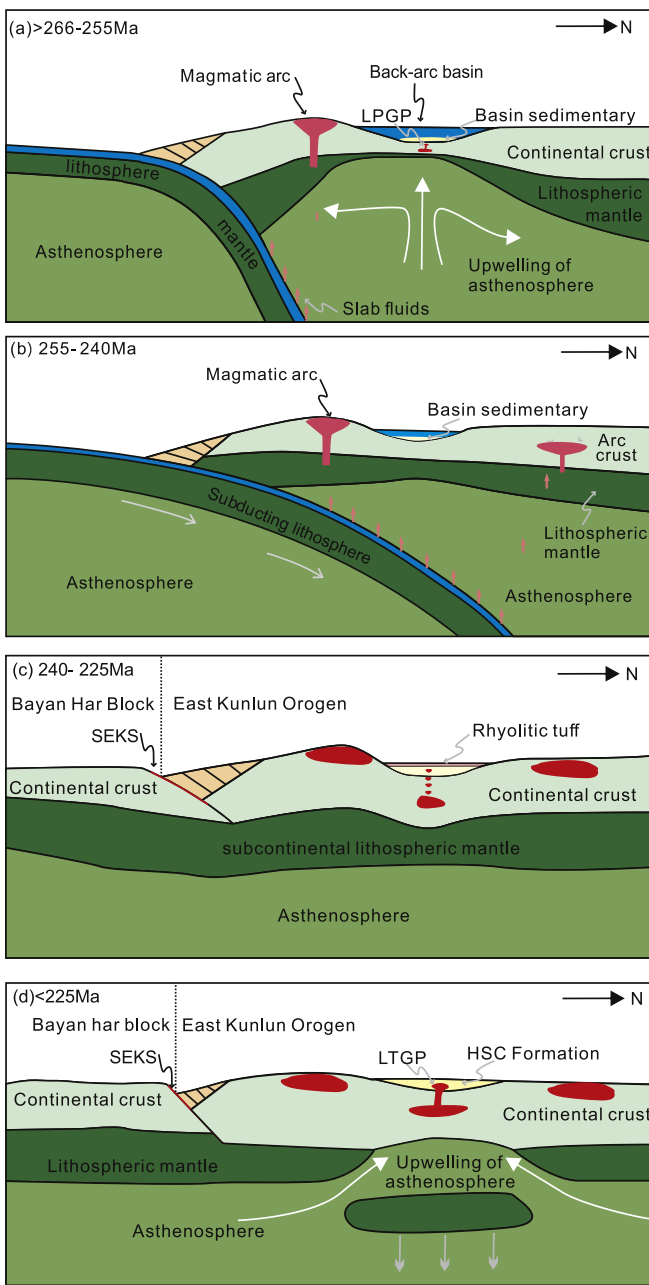


Fig. 13. Schematic model showing the tectonic evolution of the Paleo-Tethys Ocean in the EKO. LPGP: Late Permian granite porphyry; LTGP: Late Triassic granite porphyry.

Declaration of Competing Interest

The authors declare that they have no known competing financial interests or personal relationships that could have appeared to influence the work reported in this paper.

Acknowledgments

We thank Prof. Gregory Shellnut, Editor-in-Chief and two anonymous referees for critical comments which helped in improving our manuscript. This research was jointly supported by the National Natural Science Foundation of China (41972086), the Fundamental Research Funds for the Central Universities, China University of Geosciences (Wuhan) (CUGL17043), and the China Geological Survey (12120114081401, 12120114000701). We also thank the valuable help of Yujing Zhao, Yang Tang, and Junlin Chen during the fieldwork.

Appendix A. Supplementary data

Supplementary data to this article can be found online at <https://doi.org/10.1016/j.lithos.2020.105446>.

References

- Barbarin, B., 1999. A review of the relationships between granitoid types, their origins and their geodynamic environments. *Lithos* 46, 605–626.
- Bea, F., 2012. The sources of energy for crustal melting and the geochemistry of heat-producing elements. *Lithos* 153, 278–291.
- Blichert-Toft, J., Albarède, F., 1997. Separation of Hf and Lu for high-precision isotope analysis of rock samples by magnetic sector-multiple collector ICP-MS. *Contrib. Mineral. Petrol.* 127, 248–260.
- Bonin, B., 2007. A-type granites and related rocks: evolution of a concept, problems and prospects. *Lithos* 97, 1–29.
- Chappell, B.W., 1999. Aluminium saturation in I- and S-type granites and the characterization of fractionated haplogranites. *Lithos* 46, 535–551.
- Chen, L., Sun, Y., Pei, X.Z., Gao, M., Tao, F., Zhang, Z.Q., Chen, W., 2001. Northernmost Paleo-Tethyan oceanic basin in Tibet: geochronological evidence from ^{40}Ar - ^{39}Ar age dating of Dur'ngoi ophiolite. *Chin. Sci. Bull.* 46, 1203–1205.
- Chen, L., Sun, Y., Pei, X.Z., Feng, T., Zhang, G.W., 2004. Comparison of eastern paleo-Tethyan ophiolites and its geodynamic significance: Evidence from the Dur'ngoi ophiolite. *Science in China. Earth Sci.* 47, 378–384 (in Chinese with English abstract).
- Chen, N.S., Li, X.Y., Zhang, K.X., Wang, G.C., Zhu, Y.H., Hou, G.J., Bai, Y.S., 2006. Lithological Characteristics of the Baishahe Formation to the South of Xiangride Town, Eastern Kunlun Mountains and its age constrained from Zircon Pb-Pb Dating. *Geol. Sci. Technol. Inform.* 25, 1–7 (in Chinese with English abstract).
- Chen, X.H., Gehrels, G., An, Y., Li, L., Jiang, R.B., 2012. Paleozoic and Mesozoic basement magmatism of Eastern Qaidam Basin, Northern Qinghai-Tibet Plateau: LA-ICP-MS zircon U-Pb geochronology and its geological significance. *Acta Geol. Sin.* 86, 350–369.
- Chen, G.C., Pei, X.Z., Li, R.B., Li, Z.C., Pei, L., Liu, Z.Q., Chen, Y.X., Liu, C.J., Gao, J.M., Wei, F.H., 2013. Zircon U-Pb geochronology, geochemical characteristics and geological significance of Cocoe A'long Quartz Diorites Body from the Hongshuichuan Area in East Kunlun. *Acta Geol. Sin.* 87, 178–196 (in Chinese with English abstract).
- Chen, J.J., Fu, L.B., Wei, J.H., Tian, N., Xiong, L., Zhao, Y.J., Zhang, Y.J., Qi, Y.Q., 2016. Geochemical characteristics of the Late Ordovician granodiorite in the Gouli area, Eastern Kunlun Orogenic Belt, Qinghai Province: Implications on the evolution of the Proto-Tethys Ocean. *Earth Sci. J. China Univ. Geosci.* 41, 1863–1882 (in Chinese with English abstract).
- Chen, J.J., Wei, J.H., Fu, L.B., Li, H., Zhou, H.H., Zhao, X., Zhan, X.F., Tan, J., 2017. Multiple sources of the early Mesozoic Gouli batholith, eastern Kunlun Orogenic Belt, northern Tibetan plateau: linking continental crustal growth with oceanic subduction. *Lithos* 292–293, 161–178.
- Clemens, J.D., 2003. S-type granitic magmas-petrogenetic issues, models and evidence. *Earth-Sci. Rev.* 61, 1–18.
- Collins, W.J., Richards, S.W., 2008. Geodynamic significance of S-type granites in circum-Pacific orogens. *Geology* 36, 559–562.
- Collins, W.J., Beams, S.D., White, A.J.R., 1982. Nature and origin of A-type granites with particular reference to southeastern Australia. *Contrib. Mineral. Petrol.* 80, 189–200.
- Collins, W.J., Huang, H.Q., Jiang, X.Y., 2016. Water-fluxed crustal melting produces Cordilleran batholiths. *Geology* 44, 143–146.
- Dai, J.G., Wang, C.S., Hourigan, J., Santosh, M., 2013. Multi-stage tectono-magmatic events of the Eastern Kunlun Range, northern Tibet: Insights from U-Pb geochronology and (U-Th)/He thermochronology. *Tectonophysics* 599, 97–106.
- Deng, J.F., Feng, Y.F., Di, Y.J., Liu, C., Xiao, Q.H., Shu, S.G., Zhao, G.C., Meng, F., Ma, S., Yao, T., 2015. Magmatic arc and ocean-continent transition: discussion. *Geol. Rev.* 61, 473–484 (in Chinese with English abstract).
- Ding, S., Huang, H., Niu, Y.N., Zhao, Z.D., Yu, X.H., Mo, X.X., 2011. Geochemistry, geochronology and petrogenesis of East Kunlun high Nb-Ta rhyolites. *Acta Petrol. Sin.* 27, 3603–3614 (in Chinese with English abstract).
- Dobosi, G., Kempton, P.D., Downes, H., Embrey-Iszttin, A., Thirlwall, M., Greenwood, P., 2003. Lower crustal granulite xenoliths from the Pannonian Basin, Hungary, part 2: Sr-Nd-Pb-Hf and O isotope evidence for formation of continental lower crust by tectonic emplacement of oceanic crust. *Contrib. Mineral. Petrol.* 144, 671–683.
- Dong, Y.P., He, D.F., Sun, S.S., Liu, X.M., Zhou, X.H., Zhang, F.F., Yang, Z., Cheng, B., Zhao, G.C., Li, J.H., 2018. Subduction and accretionary tectonics of the East Kunlun orogen, western segment of the Central China Orogenic System. *Earth Sci. Rev.* 186, 231–261.
- Douce, A.E.P., 1999. What do experiments tell us about the relative contributions of crust and mantle to the origins of granitic magmas? In: Castro, A., Fernandez, C., Vigneresse, J.L. (Eds.), *Understanding Granites: Integrating New and Classical Techniques*. Geological Society of London, Special Publications vol. 168, pp. 55–75.
- Feng, J.Y., Pei, X.Z., Yu, S.L., Ding, S.P., Li, R.B., Sun, Y., Zhang, Y.F., Li, Z.C., Chen, Y.X., Zhang, X.F., Chen, G.C., 2010. The discovery of the mafic-ultramafic melange in Kekesha area of Dulan County, East Kunlun region, and its LA-ICP-MS zircon U-Pb age. *Geol. China* 37, 28–38 (in Chinese with English abstract).
- Gao, Y.B., Li, W.Y., Ma, X.G., Zhang, Z.W., Tang, Q.Y., 2012. Genesis, geochronology and Hf isotopic compositions of the magmatic rocks in Galige iron deposit, eastern Kunlun. *J. Lanzhou Univ.* 48, 36–47 (in Chinese with English abstract).
- Gao, P., Zheng, Y.F., Zhao, Z.F., 2016. Experimental melts from crustal rocks: A components constraint on granite petrogenesis. *Lithos* 266–277, 133–157.

- Griffin, W.L., Pearson, N.J., Belousova, E., Jackson, S.E., van Achterbergh, E., O'Reilly, S.Y., Shee, S.R., 2000. The Hf isotope composition of cratonic mantle: LAM-MC-ICPMS analysis of zircon megacrysts in kimberlites. *Geochim. Cosmochim. Acta* 64, 133–147.
- Harris, N.B.W., Xu, R.H., Lewis, C.L., Jin, C., 1988. Plutonic rocks of the 1985 Tibet geotraverse, Lhasa to Golmud. *Phil. Trans. R. Soc. Lond. A* 327, 145–168.
- He, D.F., Dong, Y.P., Liu, X.M., Yang, Z., Sun, S.S., Cheng, B., Li, W., 2016. Tectono-thermal events in East Kunlun, Northern Tibetan Plateau: Evidence from zircon U-Pb geochronology. *Gondwana Res.* 30, 179–190.
- Hoskin, P.W.O., Schaltegger, U., 2003. The composition of zircon and igneous and metamorphic petrogenesis. *Rev. Mineral. Geochem.* 53, 27–62.
- Hu, Y., Niu, Y.L., Li, J.Y., Ye, L., Kong, J.J., Chen, S., Zhang, Y., Zhang, G.R., 2016. Petrogenesis and tectonic significance of the late Triassic mafic dikes and felsic volcanic rocks in the East Kunlun Orogenic Belt, Northern Tibetan Plateau. *Lithos* 245, 205–222.
- Huang, H., Niu, Y.L., Nowell, G., Zhao, Z.D., Yu, X.H., Zhu, D.C., Mo, X.X., Ding, S., 2014. Geochemical constraints on the petrogenesis of granitoids in the East Kunlun Orogenic belt, northern Tibetan Plateau: Implications for continental crust growth through syn-collisional felsic magmatism. *Chem. Geol.* 370, 1–18.
- Janoušek, V., Finger, F., Roberts, M., Frýda, J., Pin, C., Dolejš, D., 2004. Deciphering the petrogenesis of deeply buried granites: whole-rock geochemical constraints on the origin of largely undepleted felsic granulites from the Moldanubian Zone of the Bohemian Massif. *Trans. R. Soc. Edinb.* 389, 141–159.
- Jia, X.H., Wang, Q., Tang, G.J., 2009. A-type granites: research progress and implications. *Geotecton. Metallog.* 33, 465–480 (in Chinese with English abstract).
- Jiao, S.J., Li, X.H., Huang, H.Q., Deng, X.G., 2015. Metasedimentary melting in the formation of charnockite: petrological and zircon U-Pb-Hf-O isotope evidence from the Darongshan S-type granitic complex in southern China. *Lithos* 239, 217–233.
- Jin, L.J., Zhou, H.W., Zhu, Y.H., Lin, Q.X., 2015. U-Pb Age of the Detrital Zircon from the Serteng Formation in East Kunlun: Constraints on its Provenance and Formation Time. *Geotecton. Metallog.* 33, 691–703 (in Chinese with English abstract).
- Kempton, P.D., McGill, R., 2002. Procedures for the analysis of common lead at the NERC Isotope Geosciences Laboratory and an assessment of data quality. *NIGL Rep. Ser.* 178, 1–60.
- Koester, E., Pawley, A.R., Fernandes, L.A.D., Porcher, C.C., Jr, S.E., 2002. Experimental melting of cordierite gneiss and the petrogenesis of syntranscurrent peraluminous granites in southern Brazil. *J. Petrol.* 43, 1595–1616.
- Kong, H.L., Li, J.C., Li, Y.Z., Jiao, Q.Z., Guo, X.Z., 2017. Zircon LA-ICP-MS U-Pb dating and its geological significance of the Jiadang gabbro in the eastern section of East Kunlun, Qinghai Province. *Geol. Explor.* 53, 889–902 (in Chinese with English abstract).
- Li, R.B., 2012. Research on the Late Paleozoic-Early Mesozoic orogeny in East Kunlun Orogen. (Doctor). Chang'an University, pp. 1–185 (in Chinese with English abstract).
- Li, B.L., Sun, F.Y., Yu, X.F., et al., 2012. U-Pb dating and geochemistry of diorite in the Eastern Section from Eastern Kunlun Middle uplifted Basement and Granitic Belt. *Acta Petrol. Sin.* 28, 1163–1172 (in Chinese with English abstract).
- Li, R.B., Pei, X.Z., Pei, L., Li, Z.C., Chen, G.C., Chen, Y.X., Liu, C.J., Wang, M., 2018. The Early Triassic Andean-type Halagatu granitoids pluton in the East Kunlun orogen, northern Tibet Plateau: Response to the northward subduction of the Paleo-Tethys Ocean. *Gondwana Res.* 62, 212–226.
- Liu, H., Zhao, J.H., 2018. Neoproterozoic peraluminous granitoids in the Jiangnan Fold Belt: Implications for lithospheric differentiation and crustal growth. *Precambrian Res.* 309, 152–165.
- Liu, Z.Q., Pei, X.Z., Li, R.B., Li, Z.C., Zhang, X.F., Liu, Z.G., Chen, G.C., Chen, Y.X., Ding, S.P., Guo, J.F., 2011. LA-ICP-MS Zircon U-Pb Geochronology of the Two Suites of Ophiolites at the Buqingshan Area of the A'nyemaqen Orogenic Belt in the Southern Margin of East Kunlun and Its Tectonic Implication. *Acta Geol. Sin.* 30, 185–194 (in Chinese with English abstract).
- Liu, J.N., Feng, C.Y., Qi, F., Li, G.C., Ma, S.C., Xiao, Y., 2012. SIMS zircon U-Pb dating and fluid inclusion studies of Xiadeboli Cu-Mo ore district in Dulan County, Qinghai Province, China. *Acta Petrol. Sin.* 28, 679–690 (in Chinese with English abstract).
- Liu, B., Ma, C.Q., Huang, J., Wang, L.X., Zhao, S.Q., Yan, R., Sun, Y., Xiong, F.H., 2017. Petrogenesis and tectonic implications of Upper Triassic apposite dykes in the East Kunlun orogenic belt, northern Tibetan Plateau. *Lithos* 284–285, 766–778.
- Lu, S.N., Yu, H.F., Zhao, F.Q., 2002. Precambrian Geology of the Northern Margin of the Tibetan Plateau. Geological Publishing House, Beijing 125p. (in Chinese).
- Lugmair, G.W., Marti, K., 1978. Lunar initial $^{143}\text{Nd}/^{144}\text{Nd}$: differential evolution of the lunar crust and mantle. *Earth Planet. Sci. Lett.* 39, 349–357.
- Luo, M.F., Mo, X.X., Yu, X.H., Li, X.W., Huang, X.F., Yu, J.C., 2014. Zircon LA-ICP-MS U-Pb age dating, petrogenesis and tectonic implications of the Late Triassic granites from the Xianggride area, East Kunlun. *Acta Petrol. Sin.* 30, 3229–3241 (in Chinese with English abstract).
- Ma, C.Q., Xiong, F.H., Yin, S., Wang, L.X., Gao, K., 2015. Intensity and cyclicity of orogenic magmatism: An example from a Paleo-Tethyan granitoid batholith, Eastern Kunlun, northern Qinghai-Tibetan Plateau. *Acta Petrol. Sin.* 31, 3555–3568 (in Chinese with English abstract).
- Middlemost, E.A.K., 1994. Naming materials in the magma/igneous rock system. *Earth-Sci. Rev.* 37, 215–224.
- Mo, X.X., Luo, Z.H., Deng, J.F., Yu, X.H., Liu, C.D., Chen, H.W., Yuan, W.M., Liu, Y.H., 2007. Granitoids and crustal growth in the East-Kunlun Orogenic Belt. *Geol. J. China Univ.* 13, 403–414 (in Chinese with English abstract).
- Niu, Y.L., Batiza, R., 1997. Trace element evidence from seamounts for recycled oceanic crust in the Eastern Pacific mantle. *Earth Planet. Sci. Lett.* 148, 471–483.
- Petford, N., Atherton, M., 1996. Na-rich partial melts from newly underplated basaltic crust: the Cordillera Blanca Batholith. *J. Petrol.* 37, 1491–1521.
- Pitcher, W.S., 1983. Granite Type and Tectonic Environment. Mountain Building Processes Academic Press, London, pp. 19–40.
- Powell, R., 1983. Processes in granulite-facies metamorphism. In: Atherton, M.P., Gribble, C.D. (Eds.), *Migmatites, Melting and Metamorphism*. Shiva, Cheshire, pp. 27–139.
- Rapp, R.P., Watson, E.B., 1995. Dehydration melting of metabasalt at 8–32 kbar: implications for continental growth and crust–mantle recycling. *J. Petrol.* 36, 891–931.
- Rudnick, R.L., Gao, S., 2003. Composition of the continental crust. *Treat. Geochem.* 3, 1–64.
- Sengör, A.M., 1979. Mid-Mesozoic closure of Permo-Triassic Tethys and its implications. *Nature* 279, 590–593.
- Söderlund, U., Patchett, P.J., Vervoort, J.D., Isachsen, C.E., 2004. The ^{176}Lu decay constant determined by Lu-Hf and U-Pb isotope systematics of Precambrian mafic intrusions. *Earth Planet. Sci. Lett.* 219, 311–324.
- Song, Z.B., Zhang, Y.L., Chen, X.D., Jiang, L., Li, D.S., Shu, X.F., Su, Y.Z., Li, J.C., Kong, H.L., 2013. Geochemical characteristics of Harizha granite diorite-porphry in East Kunlun and their geological implications. *Mineral Deposits* 32, 157–168 (in Chinese with English abstract).
- Steiger, R.H., Jäger, E., 1977. Subcommission on geochronology: convention on the use of decay constants in geo- and cosmochronology. *Earth Planet. Sci. Lett.* 36, 359–362.
- Stevens, J., Villaros, A., Moyen, J.F., 2007. Selective peritectic garnet entrainment as the origin of geochemical diversity in S-type granites. *Geology* 35, 9–12.
- Suess, E., 1981. Are great oceans depth permanent? *Nat. Sci.* 2, 180–187.
- Sun, Y., 2010. The Geological Characteristics, Age and Tectonic Environment Studies About Delishitan Ophiolites in Buqingshan, South of East Kunlun Mountain. (Doctor). Chang'an University 85p. (in Chinese with English abstract).
- Sun, S.S., McDonough, W.F., 1989. Chemical and isotopic systematics of oceanic basalts: implications for mantle composition and processes. *Geol. Soc. Lond. Spec. Publ.* 42, 313–345.
- Sylvester, P.J., 1998. Postcollisional strongly peraluminous granites. *Lithos* 45, 29–44.
- Thompson, A.B., 1983. Fluid-absent metamorphism. *J. Geol. Soc.* 140, 533–547.
- Vernon, R.H., 1984. Microgranitoid enclaves in granites-globulen of hybrid magma quenched in a plutonic environment. *Nature* 309, 438–439.
- Vervoort, J.D., Blachert-Toft, J., 1999. Evolution of the depleted mantle: hf isotope evidence from juvenile rocks through time. *Geochim. Cosmochim. Acta* 63, 533–556.
- Villaros, A., Buick, I.S., Stevens, G., 2012. Isotopic variations in S-type granites: an inheritance from a heterogeneous source? *Contrib. Mineral. Petrol.* 163, 243–257.
- Wang, G.C., Wang, Q.H., Jian, P., Zhu, Y.H., 2004. Zircon SHRIMP ages of Precambrian metamorphic basement rocks and their tectonic significance in the eastern Kunlun Mountains, Qinghai Province, China. *Earth Sci. Front.* 11, 481–490 (in Chinese with English abstract).
- Wang, G.C., Wei, Q.R., Jia, C.X., Zhang, K.X., Li, D.W., Zhu, Y.H., Xiang, S.Y., 2007. Some ideas of Precambrian geology in the East Kunlun, China. *Geol. Bull. China* 26, 929–937 (in Chinese with English abstract).
- Wang, S., Feng, C.Y., Li, S.J., Jiang, J.H., Li, D.S., Su, S.S., 2009. Zircon SHRIMP U-Pb dating of granodiorite in the Kaerqueka polymetallic ore deposit, Qimantage Mountain, Qinghai Province, and its geological implications. *Geol. China* 36, 74–84 (in Chinese with English abstract).
- Wang, G., Sun, F.Y., Li, B.Y., Li, S.J., Zhao, J.W., Yang, Q.A., 2014. Zircon U-Pb Geochronology and Geochemistry of Diorite in Xiarihamu Ore District from East Kunlun and Its Geological Significance. *J. Jilin Univ.* 44, 876–891 (in Chinese with English abstract).
- Wang, X., Chao, Y., Zhang, Y.Y., Sun, M., Wang, L.X., Soldner, J., Li, Z.F., 2018. S-type granite from the Gongpoquan arc in the Beishan Orogenic Collage, southern Altaids: Implications for the tectonic transition. *J. Asian Earth Sci.* 153, 206–222.
- Weinberg, R.F., Hasalová, P., 2015. Water-fluxed melting of the continental crust: A review. *Lithos* 212–215, 158–188.
- Whalen, J.B., 1985. Geochemistry of an Island-Arc Plutonic Suite: the Uasilau-Yau Yau Intrusive Complex. New Britain, P.N.G. *J. Petrol.* 26, 603–632.
- Whalen, J.B., Currie, K.L., Chappell, B.W., 1987. A-type granites: geochemical characteristics, discrimination and petrogenesis. *Contrib. Mineral. Petrol.* 95, 407–419.
- Workman, R.K., Hart, S.R., 2005. Major and trace element composition of the depleted MORB mantle (DMM). *Earth Planet. Sci. Lett.* 231 (1–2), 53–72.
- Wu, C., Zuza, A.V., Chen, X., Ding, L., Levy, D.A., Liu, C.F., Liu, W.C., Jiang, T., Stockli, D.F., 2019. Tectonics of the Eastern Kunlun Range: Cenozoic reactivation of a Paleozoic-early Mesozoic orogen. *Tectonics* 38, 1609–1650.
- Xia, R., 2017. Paleo-tethys orogenic process and gold metallogenesis of the East Kunlun. China Univ. Geosci. (Beijing) 1–215 (in Chinese with English abstract).
- Xia, R., Qing, M., Wang, C.M., Li, W.L., 2014. The genesis of the ore-bearing porphyry of the Tuoketu porphyry Cu-Au (Mo) deposit in the East Kunlun, Qinghai Province: Constraints from zircon U-Pb geochronological and geochemistry. *J. Jilin Univ.* 44, 1502–1524 (in Chinese with English abstract).
- Xiao, Y., Feng, C.Y., Liu, J.N., Yu, M., Zhou, J.H., Li, D.X., Zhao, Y.M., 2013. LA-MC-ICP-MS zircon U-Pb dating and sulfur isotope characteristics of Kendeke Fe-polymetallic deposit, Qinghai Province. *Mineral Deposits* 32, 177–186 (in Chinese with English abstract).
- Xiong, F.H., 2014. Spatial-Temporal Pattern, Petrogenesis and Geological Implications of Paleo-Tethyan Granitoids in the East Kunlun Orogenic Belt (Eastern Segment). (Doctor). China University of Geosciences 191 p. (in Chinese with English abstract).
- Xiong, F.H., Ma, C.Q., Zhang, J.Y., Liu, B., 2011. LA-ICP-MS zircon U-Pb dating, elements and Sr-Nd-Hf isotope geochemistry of the Early Mesozoic mafic dyke swarms in East Kunlun Orogenic belt. *Acta Petrol. Sin.* 27, 3350–3364 (in Chinese with English abstract).
- Xiong, F.H., Ma, C.Q., Hong, J.A., Liu, B., Huang, J., 2013. Multi-style modification of subcontinental lithospheric mantle during a Tethys orogeny: evidence from Permo-Triassic mafic dike swarms in Northern Tibet Plateau. *Acta Geol. Sin. (Engl. Ed.)* 87, 274–276.
- Xiong, F.H., Ma, C.Q., Zhang, J.Y., Liu, B., Jiang, H.A., 2014. Reworking of old continental lithosphere: an important crustal evolution mechanism in orogenic belts, as evidenced by Triassic I-type granitoids in the East Kunlun orogen, Northern Tibetan Plateau. *J. Geol. Soc.* 171, 847–863.
- Xiong, F.H., Ma, C.Q., Chen, B., Ducea, M.N., Hou, M.C., Ni, S.J., 2019. Intermediate-mafic dikes in the East Kunlun Orogen, Northern Tibetan Plateau: a window into paleo-arc magma feeding system. *Lithos* 340–341, 152–165.

- Xu, Z.Q., Dilek, Y., Cao, H., Yang, J.S., Robinson, P., Ma, C.Q., Li, H.Q., Jolivet, M., Roger, F., Chen, X.J., 2015. Paleo-Tethyan evolution of Tibet as recorded in the East Cimmerides and West Cathaysides. *J. Asian Earth Sci.* 105, 320–337.
- Yang, J.S., Robinson, P.T., Jiang, C.F., Xu, Z.Q., 1996. Ophiolites of the Kunlun Mountains, China and their tectonic implications. *Tectonophysics* 258, 215–231.
- Yin, A., Harrison, M., 2000. Geologic Evolution of the Himalayan-Tibetan Orogen. *Annu. Rev. Earth Planet. Sci.* 28, 211–280.
- Yin, L.J., Liu, H.J., Yang, L.G., Liu, W.M., 2013. Geochronology, geochemistry and geological significance of granites from the Baishiya skarn iron-polymetallic deposit, Dulan, Qinghai Province. *Xinjiang Geol.* 31, 248–255 (in Chinese with English abstract).
- Yu, M., Feng, C.Y., Zhao, Y.M., Li, D.X., 2015. Genesis of post-collisional calc-alkaline and alkaline granitoids in Qiman Tagh, East Kunlun, China. *Lithos* 239, 45–59.
- Zhang, G., 2012. Research on geological characteristics, ages and geological significance of the Halagatu granitic rocks in east segment of the East Kunlun Orogen. (Doctor). Chang'an University 82 p. (in Chinese with English abstract).
- Zhang, J.X., Meng, F.C., Wan, Y.S., Yang, J.S., Dong, G.A., 2003. Early Paleozoic tectono-thermal event of the Jinshui Group on the southern margin of Qaidam: Zircon U-Pb SHRIMP age evidence. *Geol. Bull. China* 22, 397–404 (in Chinese with English abstract).
- Zhao, X., Fu, L.B., Wei, J.H., Zhao, Y.J., Tang, Y., Yang, B.R., Guan, B., Wang, X.Y., 2018. Geochemical characteristics of the An'nage hornblende gabbro from East Kunlun Orogenic Belt: Constraints on the evolution of Paleo-Tethys Ocean. *Earth Sci. J. China Univ. Geosci.* 43, 354–370 (in Chinese with English abstract).
- Zhao, X., Fu, L.B., Wei, J.H., Bagas, L., Santosh, M., Liu, Y., Zhang, D.H., Zhou, H.Z., 2019. Late Permian back-arc extension of the eastern Paleo-Tethys Ocean: Evidence from the East Kunlun Orogen, northern Tibetan Plateau. *Lithos* 340–341, 34–48.
- Zhu, R.Z., Lai, S.C., Qin, J.F., Zhao, S.W., Santosh, M., 2018. Strongly peraluminous fractionated S-type granites in the Baoshan Block, SW China: Implications for two-stage melting of fertile continental materials following the closure of Bangong-Nujiang Tethys. *Lithos* 316–317, 178–198.